Monthly Notices
of the
ROYAL ASTRONOMICAL SOCIETY

MNRAS **495,** 4747–4768 (2020)
Advance Access publication 2020 May 22

doi:10.1093/mnras/staa1423

High-redshift *JWST* predictions from IllustrisTNG: II. Galaxy line and continuum spectral indices and dust attenuation curves

Xuejian Shen,[1]★ Mark Vogelsberger,[2] Dylan Nelson,[3] Annalisa Pillepich,[4] Sandro Tacchella,[5] Federico Marinacci,[6] Paul Torrey,[7] Lars Hernquist[5] and Volker Springel[3]

[1]*TAPIR, California Institute of Technology, Pasadena, CA 91125, USA*
[2]*Department of Physics, Kavli Institute for Astrophysics and Space Research, Massachusetts Institute of Technology, Cambridge, MA 02139, USA*
[3]*Max-Planck-Institut für Astrophysik, Karl-Schwarzschild-Str 1, D-85748 Garching, Germany*
[4]*Max-Planck-Institut für Astronomie, Königstuhl 17, D-69117 Heidelberg, Germany*
[5]*Harvard-Smithsonian Center for Astrophysics, 60 Garden Street, Cambridge, MA 02138, USA*
[6]*Department of Physics & Astronomy, University of Bologna, via Gobetti 93/2, I-40129 Bologna, Italy*
[7]*Department of Astronomy, University of Florida, 211 Bryant Space Sciences Center, Gainesville, FL 32611, USA*

Accepted 2020 May 19. Received 2020 May 19; in original form 2020 February 24

ABSTRACT

We present predictions for high redshift ($z = 2-10$) galaxy populations based on the IllustrisTNG simulation suite and a full Monte Carlo dust radiative transfer post-processing. Specifically, we discuss the Hα and Hβ + [O III] luminosity functions up to $z = 8$. The predicted Hβ + [O III] luminosity functions are consistent with present observations at $z \lesssim 3$ with $\lesssim$0.1 dex differences in luminosities. However, the predicted Hα luminosity function is $\sim$0.3 dex dimmer than the observed one at $z \simeq 2$. Furthermore, we explore continuum spectral indices, the Balmer break at 4000 Å; (D4000) and the UV continuum slope β. The median D4000 versus specific star formation rate relation predicted at $z = 2$ is in agreement with the local calibration despite a different distribution pattern of galaxies in this plane. In addition, we reproduce the observed $A_{\rm UV}$ versus β relation and explore its dependence on galaxy stellar mass, providing an explanation for the observed complexity of this relation. We also find a deficiency in heavily attenuated, UV red galaxies in the simulations. Finally, we provide predictions for the dust attenuation curves of galaxies at $z = 2-6$ and investigate their dependence on galaxy colours and stellar masses. The attenuation curves are steeper in galaxies at higher redshifts, with bluer colours, or with lower stellar masses. We attribute these predicted trends to dust geometry. Overall, our results are consistent with present observations of high-redshift galaxies. Future *James Webb Space Telecope* observations will further test these predictions.

Key words: methods: numerical – galaxies: high redshift – galaxies: evolution – galaxies: formation – ultraviolet: galaxies.

1 INTRODUCTION

The ΛCDM model (e.g. Planck Collaboration XIII 2016), as the concordant paradigm of structure formation, provides a framework for the assembly of dark matter haloes where galaxies form. The current theory of galaxy formation (White & Rees 1978; Blumenthal et al. 1984) makes further testable predictions for observed galaxy populations. Comparing these predictions with observations at multiple epochs of cosmic evolution is important for confirming or falsifying the theory. Despite the well-studied observational constraints in the local Universe, observations of high-redshift galaxy populations offer a unique and much less explored channel to test the current theory of structure formation (see reviews of Shapley 2011; Stark 2016; Dayal & Ferrara 2018, and references therein).

Much effort has been devoted to the study of high-redshift galaxy populations with both space- and ground-based facilities. For the selection of galaxies, the Lyman-break technique was extended to $z \gtrsim 6$ (e.g. Bouwens et al. 2003; Stanway, Bunker & McMahon 2003; Yan, Windhorst & Cohen 2003) with the Advanced Camera for Surveys on the *Hubble Space Telescope* (*HST*). The Wide-Field

★ E-mail: xshen@caltech.edu

Camera 3 with near-IR filters on the *HST* further advanced the search for star-forming galaxies beyond $z = 7$ (e.g. Bouwens et al. 2010; Oesch et al. 2010; Wilkins et al. 2010; McLure et al. 2013; Finkelstein et al. 2015). Currently, deep field extragalactic surveys performed with the *HST* have enabled measurements of the galaxy rest-frame UV luminosity function to $z \sim 10$ (e.g. Ishigaki et al. 2018; Oesch et al. 2018; Bouwens et al. 2019). By combining observations from the *HST*, the *Spitzer Space Telescope* and other ground-based facilities, broad-band photometric spectral energy distributions (SEDs) of thousands of galaxies up to $z = 8$ (e.g. Eyles et al. 2005; González et al. 2010; Stark et al. 2013; Duncan et al. 2014; Song et al. 2016) have been measured to study the assembly of galaxy stellar populations at high redshift. Meanwhile, high resolution spectroscopic observations of galaxies have been conducted beyond $z \simeq 2-3$ (e.g. Keck/MOSFIRE: Steidel et al. 2014; Kriek et al. 2015; Strom et al. 2017) and have revealed the physical state of galaxies at high redshift. In addition, far-IR and submillimeter observations revealed a population of highly obscured star-forming galaxies at $z \gtrsim 2$ (e.g. Blain et al. 2002; Solomon & Vanden Bout 2005; Weiß et al. 2009; Hodge et al. 2013; Simpson et al. 2014; da Cunha et al. 2015; Simpson et al. 2015) and have expanded our knowledge of galaxy formation and dust physics at high redshift.

Despite these successes, measurements of physical properties of galaxies at high redshift, such as the stellar mass and the SFR, are still very uncertain (e.g. Papovich, Dickinson & Ferguson 2001; Marchesini et al. 2009; Behroozi, Conroy & Wechsler 2010; Wuyts et al. 2011; Speagle et al. 2014; Mobasher et al. 2015; Santini et al. 2015; Leja et al. 2019). Detection of galaxy emission at longer wavelengths than the rest-frame UV is hindered by the limited wavelength coverage of the *HST*, the insufficient sensitivity of infrared (IR) instruments, and the atmospheric blocking of ground-based observations. Due to these limitations, the physical properties and evolution of dust, which mainly emits in the IR, are also largely unexplored at high redshift. Dust attenuation generates additional uncertainties in the interpretation of observations. The upcoming *James Webb Space Telecope* (*JWST*; Gardner et al. 2006) will offer access to galaxy optical and IR emission beyond the current redshift frontier. The near-IR camera (NIRCam) and the mid-IR instrument on *JWST* are designed to obtain broad-band photometry over the wavelength range from 0.7 to 25.5μm with unprecedented sensitivity. *JWST* will extend observations of the galaxy rest-frame UV luminosity function to higher redshift ($z > 10$) and fainter luminosity. It will also allow detection of optical and near-IR (NIR) SEDs of high-redshift galaxies. The near-IR spectrograph (NIRSpec) will enable high-resolution spectroscopy of distant galaxies and precise measurements of spectral indices, such as emission line luminosities, line ratios, and breaks in the continuum flux. These instrumental advances will provide new insights in both the formation and evolution of high-redshift galaxy populations and dust physics.

In parallel to the observational efforts, various theoretical works have made predictions for high-redshift galaxy populations. This has included empirical models (e.g. Tacchella, Trenti & Carollo 2013; Mason, Trenti & Treu 2015; Tacchella et al. 2018), semi-analytical models for galaxy formation (e.g. Cowley et al. 2018; Yung et al. 2019a,b), and hydrodynamical simulations. For example, the First Billion Years simulation suite (e.g. Paardekooper, Khochfar & Dalla 2013), the BlueTides simulation (e.g. Wilkins et al. 2016, 2017), the Renaissance simulation suite (e.g. Xu et al. 2016; Barrows et al. 2017), the FirstLight simulation (e.g. Ceverino, Glover & Klessen 2017), the FIRE-2 simulation suite (e.g. Ma et al. 2018, 2019), the Sphinx simulation (Rosdahl et al. 2018), and others (e.g. Dayal et al. 2013; Shimizu et al. 2014; Wu et al. 2019). However, we note that most of these hydrodynamical simulations have only been evolved down to relatively high redshift due to computational limitations. Therefore, the reliability of the high-redshift predictions from these works has not been fully justified,[1] given that these models cannot be tested at lower redshift where rich observational constraints are available. To fill this gap, we present high-redshift predictions from the IllustrisTNG simulation suite. The simulations have successfully produced a realistic low redshift Universe that is consistent with a wide range of observations. Our method combines the simulations with full Monte Carlo radiative transfer calculations to model dust attenuation. Moreover, the resolution corrections and the combination procedure introduced in Paper I (Vogelsberger et al. 2019) of this series enable predictions for galaxies over a wide dynamical range from 10^7 to $10^{12}\,M_\odot$. The technique fully utilizes the high resolution of TNG50 and the statistical power of TNG300.

In Paper I of this series, technical details of our radiative transfer post-processing procedure were introduced. Our dust attenuation model was calibrated based on the galaxy rest-frame UV luminosity functions at $z = 2-10$. The predictions for the *JWST* apparent bands' luminosity functions and number counts were presented in Paper I. As a subsequent analysis, the goal of this paper is to make further predictions for high-redshift galaxy populations that involve the $M_{\rm halo}-M_{\rm UV}$ relation, galaxy emission line luminosity functions, the Balmer break at 4000 Å; (D4000), the UV continuum slope β and its role as a dust attenuation indicator, and the dust attenuation curves. The comparisons of these predictions with existing observations demonstrate that our results are a solid guide for future observations conducted with *JWST*.

This paper is organized as follows: In Section 2, we briefly describe the IllustrisTNG simulation suite and state the numerical parameters of TNG50, TNG100, and TNG300 in detail. In Section 3, we describe the method we used to derive the dust attenuated broad-band photometry and SEDs of galaxies in the simulations. In Section 4, we briefly introduce the resolution correction and the combination procedure. The main results are presented in Section 5, where we make various predictions and comparisons with observations. Summary and conclusions are presented in Section 6.

2 SIMULATION

The analysis in this paper is based on the IllustrisTNG simulation suite (Marinacci et al. 2018; Naiman et al. 2018; Nelson et al. 2018; Pillepich et al. 2018b; Springel et al. 2018), including the newest addition, TNG50 (Pillepich et al. 2019; Nelson et al. 2019a). As the follow-up project to the Illustris simulations (Genel et al. 2014; Vogelsberger et al. 2014a,b; Nelson et al. 2015; Sijacki et al. 2015), the IllustrisTNG simulation suite consists of three primary simulations: TNG50, TNG100, and TNG300 (Nelson et al. 2019b), covering three different periodic, uniformly sampled volumes, roughly $\approx 50^3$, 100^3, 300^3 Mpc^3. The numerical parameters of these simulations are summarized in Table 1. The IllustrisTNG simulation suite

[1]The FIRE-2 simulation suite contain simulations, different from the FIRE-2 high redshift simulations (Ma et al. 2018, 2019), which have been evolved to $z = 0$ using the same physics model (Hopkins et al. 2018). So, its local Universe predictions have been tested to some level.

Table 1. IllustrisTNG simulation suite. The table shows the basic numerical parameters of the three primary IllustrisTNG simulations: simulation volume side length, number of gas cells ($N_{\rm gas}$), number of dark matter particles ($N_{\rm dm}$), baryon mass resolution ($m_{\rm b}$), dark matter mass resolution ($m_{\rm dm}$), Plummer-equivalent maximum physical softening length of dark matter and stellar particles ($\epsilon_{\rm dm,stars}$), and the minimal comoving cell softening length $\epsilon^{\rm min}_{\rm gas}$. In the following, we will refer to TNG50-1 as TNG50, TNG100-1 as TNG100 and TNG300-1 as TNG300.

IllustrisTNG Simulation	Run	Volume side length (h^{-1}Mpc)	$N_{\rm gas}$	$N_{\rm dm}$	$m_{\rm b}$ ($h^{-1}{\rm M}_\odot$)	$m_{\rm dm}$ ($h^{-1}{\rm M}_\odot$)	$\epsilon_{\rm dm,stars}$ (h^{-1}kpc)	$\epsilon^{\rm min}_{\rm gas}$ (h^{-1}kpc)
TNG300	TNG300(-1)	205	2500^3	2500^3	7.4×10^6	4.0×10^7	1.0	0.25
TNG100	TNG100(-1)	75	1820^3	1820^3	9.4×10^5	5.1×10^6	0.5	0.125
TNG50	TNG50(-1)	35	2160^3	2160^3	5.7×10^4	3.1×10^5	0.2	0.05

employs the following cosmological parameters (Planck Collaboration XIII 2016): $\Omega_{\rm m} = 0.3089$, $\Omega_{\rm b} = 0.0486$, $\Omega_\Lambda = 0.6911$, $H_0 = 100\,h\,{\rm km\,s^{-1}\,Mpc^{-1}} = 67.74\,{\rm km\,s^{-1}\,Mpc^{-1}}$, $\sigma_8 = 0.8159$, and $n_{\rm s} = 0.9667$. The simulations were carried out with the moving-mesh code AREPO (Springel 2010; Pakmor et al. 2016) combined with the IllustrisTNG galaxy formation model (Weinberger et al. 2017; Pillepich et al. 2018a), which is an update of the Illustris galaxy formation model (Vogelsberger et al. 2013; Torrey et al. 2014). We note that TNG50, TNG100, and TNG300 differ in their highest numerical resolution as listed in Table 1. In the following, we will refer to TNG50-1 as TNG50, TNG100-1 as TNG100, and TNG300-1 as TNG300.

3 GALAXY LUMINOSITIES AND SEDS

In this section, we will introduce our method of deriving the intrinsic and dust attenuated galaxy luminosities and SEDs. We will follow the Model C procedure introduced in Paper I. We will briefly review the procedure and refer the readers to Paper I for details. We assigned intrinsic emission to stellar particles in the simulations using the stellar population synthesis method and post-process the intrinsic emission from stellar particles with full Monte Carlo radiative transfer calculations to model dust attenuation. To be specific, we adopt the Flexible Stellar Population Synthesis (FSPS) code (Conroy, Gunn & White 2009; Conroy & Gunn 2010) to model the intrinsic SEDs of old stellar particles (age > 10 Myr) and the MAPPINGS-III SED library (Groves et al. 2008) to model those of young stellar particles (age < 10 Myr). The MAPPINGS-III SED library self-consistently considers the dust attenuation in the birth clouds of young stars that cannot be properly resolved in the simulations. In theory, sufficiently ionized gas cells resolved in the simulations should also have some emissivities. However, self-consistently modelling this effect is beyond the scope of this paper and we did not include it in the radiative transfer post-processing. After characterizing the source, we perform the full Monte Carlo dust radiative transfer calculations using a modified version of the publicly available SKIRT (version 8)[2] code (Baes et al. 2011; Camps, Baes & Saftly 2013; Saftly, Baes & Camps 2014; Camps & Baes 2015). Modifications were made to incorporate the FSPS SED templates into SKIRT. Photon packages are then randomly released based on the source distribution characterized by the positions and SEDs of stellar particles. We have designed a specific wavelength grid for the radiative transfer calculations. The grid has 1168 grid points covering the wavelength range from 0.05 to 5μm and has been refined around emission lines.

The emitted photon packages will further interact with the dust in the interstellar medium (ISM). We assume a Draine & Li (2007) dust mixture of amorphous silicate and graphitic grains, including varying amounts of polycyclic aromatic hydrocarbons particles. This dust model is widely used (e.g. Jonsson, Groves & Cox 2010; Baes et al. 2011; Kimm & Cen 2013; Rémy-Ruyer et al. 2014), and it can reproduce the extinction properties in the Milky Way. Since we have fixed the dust model, the predictions we make in this paper will not cover the potential evolution of the physical properties of dust at high redshift. Instead, we will focus on the influence of dust geometry on dust attenuation. To determine the distribution of dust in the ISM, we consider cold gas cells (star-forming or with temperature <8000 K) from the simulations and calculate the metal mass distribution based on their metallicities. We assume that dust is traced by metals in the ISM and adopt a constant dust-to-metal ratio among all galaxies at a fixed redshift. The dust-to-metal ratios at different redshifts are calibrated based on the galaxy rest-frame UV luminosity functions at $z = 2{-}10$ (e.g. McLure et al. 2009; Ouchi et al. 2009; Bouwens et al. 2016; Finkelstein 2016; Oesch et al. 2018). We find that the redshift evolution of the dust-to-metal ratio can be well characterized by a $0.9 \times (z/2)^{-1.92}$ power law at $z = 2{-}10$ (see Paper I for the calibration procedure and a detailed discussion of the redshift dependence of the dust-to-metal ratio). We then turn the metal mass distribution into a dust mass distribution with the dust-to-metal ratio and map the dust distribution on to an adaptively refined grid. The grid is refined with an octree algorithm to maintain the fraction of dust mass within each grid cell to be smaller than 2×10^{-6}. The maximum refinement level is also adjusted to match the numerical resolution of the simulations.

Ultimately, after photons fully interacted with dust in the galaxy and escaped, they are collected by a mock detector 1 pMpc[3] away from the simulated galaxy along the positive z-direction of the simulation coordinates. The integrated galaxy flux is then recorded, which provides us with the dust attenuated SED of the galaxy in the rest frame. Galaxy SEDs without the resolved dust attenuation are derived in the same way with no resolved dust distribution imported. We note that we use the term 'without the resolved dust' because the unresolved dust component in the MAPPINGS-III SED library is always present. Compared with the resolved dust attenuation, the impact of the unresolved dust attenuation on galaxy continuum emission is limited. In order to get broad-band photometry, the galaxy SEDs are convolved with the transmission curves using the SEDPY[4] code. For the calculation of apparent magnitudes, the rest-frame flux is redshifted, corrected for the IGM absorption (Madau 1995; Madau et al. 1996), and converted to the observed spectra.

[2] http://www.skirt.ugent.be/root/_landing.html

[3] Physical Mpc.

[4] https://github.com/bd-j/sedpy

Since some predictions in this paper are concerning nebular emission line luminosities, we need to discuss the nebular emission model adopted in the MAPPINGS-III SED library in Groves et al. (2008) in more detail. The SED library adopts 1D photoionization and radiative transfer calculations to model the radiation from a newly formed massive stellar cluster. The radiation propagates through the surrounding spherically symmetrical H II region and photodissociation region (PDR). The covering fraction of the PDR decreases as a function of time as it is cleared away by the strong winds from the massive stellar cluster. The MAPPINGS-III SED of a specific young stellar particle (age < 10 Myr) is controlled by five parameters that we have chosen in the following way: (i) *Star Formation Rate:* The star formation rate (SFR) is required since the MAPPINGS-III SED templates are normalized to have SFR $= 1\,\mathrm{M}_\odot\,\mathrm{yr}^{-1}$. We assume SFR $= \mathrm{m_i}/10\,\mathrm{Myr}$ to maintain the conservation of stellar mass, where m_i is the initial mass of the young stellar particle. (ii) *Metallicity of the birth cloud:* The metallicity of the birth cloud is assumed to be the initial metallicity of the stellar particle inherited from its parent gas cell(s). This represents the metallicity of the birth environment of the stellar particle. (iii) *Pressure of the surrounding ISM:* Tracing the pressure of the stellar particle's birth environment is technically difficult in post-processing. However, as demonstrated in Groves et al. (2008), the impact of the ISM pressure on the UV to NIR continuum spectra is negligible. We therefore simply employ a fixed typical value of $\log(P_0/k_\mathrm{B})/\,\mathrm{cm}^{-3}\mathrm{K} = 5$ (Groves et al. 2008; Rodriguez-Gomez et al. 2018). The pressure does have an influence on the emission line luminosities. However, we have found that varying the pressure by an order of magnitude from the fiducial value will only lead to $\lesssim$0.1 dex differences in the luminosities of the emission lines we study in this paper. (iv) *The compactness of the birth cloud:* This describes the density of the H II region and can be calculated as $\log C = 3/5 \log M_\mathrm{cl}/\,\mathrm{M}_\odot + 2/5 \log P_0/k_\mathrm{B}/(\mathrm{cm}^{-3}\mathrm{K})$ (Groves et al. 2008), where M_cl is the mass of the stellar cluster and P_0 is the pressure of the HII region. Again, correctly deriving the properties of the stellar cluster is difficult in post-processing and may require artificial resampling. However, the compactness parameter mainly affects the temperature of dust and its emission in the FIR. It has almost no impact on the UV to NIR photometric properties (Groves et al. 2008). We therefore also fix this to a typical value of $\log C = 5$ (Groves et al. 2008; Rodriguez-Gomez et al. 2018). For the emission line luminosities, varying the compactness by an order of magnitude from the fiducial value leads to $\lesssim$0.1 dex differences in the Hα and Hβ luminosities and $\lesssim$0.25 dex difference in the [O III] luminosity. (v) *PDR covering fraction:* This defines the time-averaged fraction of the stellar cluster solid angle that is covered by the PDR. The MAPPINGS-III SED library consists of SEDs with fully covered or uncovered H II regions. The final output SED is a linear combination of these two extreme cases controlled by the parameter f_PDR. We adopt here the fiducial value 0.2 for the f_PDR (Groves et al. 2008; Jonsson et al. 2010; Rodriguez-Gomez et al. 2018). These parameters then fully specify the MAPPINGS-III SED including the nebular continuum and line emission as well as the unresolved dust attenuation in the birth clouds of young stars. This model allows us to make robust predictions for the emission line luminosities within the uncertainties quoted. As stated in Paper I, at $z \geq 6$, the young stellar populations were modelled by the FSPS SED instead of the MAPPINGS-III SED. The nebular emission at these redshifts is therefore also modelled by the FSPS code with default parameter settings. As illustrated in the calibration procedure of Paper I, this switch removes the unresolved dust component at $z \geq 6$ where its impact should be limited,[5] and leads to a better agreement in the rest-frame UV luminosity function with observations at $z \geq 6$.

As discussed in Paper I, we define a galaxy as being either a central or satellite galaxy identified by the SUBFIND algorithm (Springel et al. 2001; Dolag et al. 2009). In our analysis, we only consider galaxies with stellar mass larger than 100 times the baryonic mass resolution of the simulation, $100 \times m_\mathrm{b}$, within twice the stellar half mass radius. Galaxies below this mass threshold will not be considered in the following analysis since we assume that their structures are not reliably modelled. Furthermore, galaxy luminosities, magnitudes, stellar masses, and SFRs are all calculated within a fixed physical aperture of 30 pkpc (e.g. Pillepich et al. 2018b) and are based on gravitationally bound particles and cells only.

4 RESOLUTION CORRECTION AND COMBINATION PROCEDURE

As discussed in Paper I, our high-redshift predictions depend on the combination of TNG50, TNG100, and TNG300 simulations, which have different simulation volumes and numerical resolutions. To combine them together, a resolution correction procedure is needed for TNG100 and TNG300 simulation results to match the numerical resolution of TNG50, which provides the highest numerical resolution of the IllustrisTNG simulation suite. To be more specific, to resolution correct an arbitrary physical quantity X, for each simulation, we first divide galaxies into 20 logarithmically uniformly spaced halo mass bins ranging from 10^9 to $10^{14}\,\mathrm{M}_\odot$. Here, we assume that the halo mass is a robust quantity against numerical resolution. This assumption is supported by the fact that the halo mass functions from different simulations overlap perfectly in overlapping dynamical ranges. In each halo mass bin, we then calculate for each simulation the median X of galaxies. By comparing the median X of TNG100 (TNG300) with the median X of TNG50, we can derive the correction factor[6] of the physical quantity X for TNG100 (TNG300) to the resolution level of TNG50 at a given halo mass. The simulation volume of TNG50 is too small to provide a large number of galaxies with large halo masses. We therefore do not apply the correction once the number of galaxies in a halo mass bin drops below 10 for TNG50. This approach is supported by the fact that TNG100 and TNG300 have nearly identical galaxy luminosity (stellar mass) functions at the bright (massive) end. We can therefore safely assume a vanishing correction in this regime. We apply this whole procedure of deriving correction factors at all redshifts of interest. The resulting correction factors as a function of halo mass and redshift were stored such that we can easily correct arbitrary physical quantities at any redshift.

This resolution correction procedure has been applied to all physical quantities studied in this paper. We use these resolution corrected quantities to derive statistical distributions (e.g. luminosity functions) and scaling relations (e.g. the M_halo–M_UV relation). It is therefore by construction that all of the distributions and relations derived from the three simulations agree well in their

[5]The calibrated dust-to-metal ratio of the resolved dust component drops at higher redshift, so the unresolved dust attenuation should presumably also become weaker at higher redshift.

[6]The correction factor is an additive factor if the quantity X is the logarithm of a physical quantity, e.g. magnitudes. In other cases, it is a multiplicative factor.

shared dynamical ranges after the resolution correction. We then perform the combination procedure to smoothly connect them to get distributions or relations over a wide dynamical range. Usually, the high-resolution simulation is superior at predicting distributions or scaling relations at the low-mass (faint) end and suffers from Poisson noise at the massive (bright) end, where results from a simulation with lower resolution but larger simulated volume are required. In doing this, in the shared dynamical range of two simulations, for an arbitrary physical quantity X (already resolution corrected) depending on another physical quantity Y, we calculate the combined X in a bin of Y as

$$X_{\rm combined}(Y) = \frac{X_{50}(Y)\,N_{50}^2 + X_{100}(Y)\,N_{100}^2 + X_{300}(Y)\,N_{300}^2}{N_{50}^2 + N_{100}^2 + N_{300}^2}, \quad (1)$$

where $N_{\#}$ refers to the number of galaxies of TNG# in the bin. The weighting $N_{\#}^2$ is chosen empirically to maintain the dominance of the simulation that has the best statistic in the bin.

5 RESULTS

In this section, we explore high-redshift predictions from the IllustricTNG simulation suite and our post-processing procedure. These high-redshift predictions involve the scaling relation between galaxy host halo mass and rest-frame UV luminosity, the $M_{\rm halo}-M_{\rm UV}$ relation; the Hα and Hβ + [O III] luminosity functions; the Balmer break at 4000 Å; (D4000) as a star formation indicator; the UV continuum slope β and its role as a dust attenuation indicator; the dust attenuation curves of galaxies and the origin of its variety. In Fig. 1, we provide a visual presentation of star-forming galaxies at $z = 2$ selected from TNG50, including the *JWST* bands synthetic images, the emission line strength maps of Hα and Hβ + [O III] and the relative differences between the strength of Hα and Hβ + [O III]. The three selected galaxies are all star-forming galaxies of stellar masses $\sim 10^{10-11}$ M$_\odot$ with apparent discs and spiral arms. The line emission preferentially originates in the star-forming regions, e.g. discs and spiral arms, compared to the sparser distribution of broad-band light. We also find that Hα is relatively stronger in the star-forming regions, while Hβ + [O III] is relatively stronger at the outskirts of the galaxies. This phenomenon will be discussed in more detail in Section 5.2.3.

5.1 $M_{\rm halo}-M_{\rm UV}$ relation

Understanding the formation and evolution of high-redshift galaxies is one of the most important topics that *JWST* will help explore (e.g. Gardner et al. 2006; Cowley et al. 2018; Williams et al. 2018; Yung et al. 2019a). The evolution of galaxies during this epoch is related to the evolution of their host dark matter haloes, which naturally leads to statistical correlations between various galaxy and halo properties, known as 'galaxy–halo connections' (e.g. see the review of Wechsler & Tinker 2018, and references therein). These empirical relations help interpreting physical information of dark matter haloes from observed galaxy properties. Moreover, predictions of galaxy properties can be made from the evolutionary history of dark matter haloes (e.g. Conroy, Wechsler & Kravtsov 2007; Behroozi, Wechsler & Conroy 2013; Moster, Naab & White 2013; Tacchella et al. 2013, 2018) without explicitly modelling the baryonic processes of star formation. Due to accessibility in observations, the rest-frame UV luminosity of galaxies serves as an important observable in building such scaling relations. It has been demonstrated to be a good proxy for the stellar mass assembly at high redshift (e.g. Stark et al. 2013; Song et al. 2016), where direct measurement of galaxy stellar mass is limited by the sensitivity and resolution of IR instruments. In Paper I, we demonstrated that the IllustrisTNG simulation suite and our radiative transfer post-processing procedure produce galaxy rest-frame UV luminosity functions that are consistent with observations at $z = 2-10$. We have also studied the galaxy rest-frame UV luminosity versus stellar mass relation at $z \geq 4$ and found agreement with observations. In this paper, we explore the scaling relation between galaxy host halo mass and rest-frame UV luminosity (magnitude), the $M_{\rm halo}-M_{\rm UV}$ relation. Future galaxy clustering measurements with *JWST* are expected to place new constraints on this relation (e.g. Endsley et al. 2019).

In Fig. 2, we present the predicted relation between galaxy host halo mass and rest-frame UV magnitude at $z = 4$, 5, 6, 8. We note that the halo mass is here defined as the total mass of all the particles that are gravitationally bound to the host halo of the galaxy. Unless specified otherwise, the rest-frame UV magnitude, $M_{\rm UV}$, in all subsequent analysis in this paper is the dust attenuated magnitude. To derive the $M_{\rm halo}-M_{\rm UV}$ relation, we perform a binning in the UV magnitude with 23 bins linearly spaced from -16 to -24 mag. For each bin, we calculate the median $\log(M_{\rm halo}/{\rm M}_\odot)$ and the 1σ dispersion $\sigma_{\log M_{\rm halo}}$ for galaxies in TNG50, TNG100, and TNG300, respectively. We combine the median $\log(M_{\rm halo}/{\rm M}_\odot)$ or the $\sigma_{\log M_{\rm halo}}$ using equation (1) in the magnitude range shared by two or three simulations. At the faint end, where TNG100 (TNG300) does not provide sufficient resolution and therefore deviates from TNG50 (TNG100), we only use TNG50 (TNG50 and TNG100) to construct the combined $M_{\rm halo}-M_{\rm UV}$ relation. In the combination procedure, we do not consider bins with fewer than 10 galaxies in TNG300. The combined median relations are presented as the blue solid lines in Fig. 2. The error bars represent 1σ dispersions in $\log(M_{\rm halo}/{\rm M}_\odot)$. We note that all the subsequent analysis in this paper undergo similar binning and combination procedures and all the presented relations/distributions are resolution corrected and combined unless specified otherwise. Fig. 2 reveals a strong correlation between galaxy host halo mass and rest-frame UV luminosity. Dust attenuation is clearly important and it shifts the relation towards the high halo mass direction at the bright end. We compare our results with the relations predicted by empirical models (Tacchella et al. 2013, 2018; Trac et al. 2015; Endsley et al. 2019) and the simulation of Shimizu et al. (2014). The predictions are qualitatively consistent with these previous studies in that the relations monotonically increase and exhibit a steepening induced by the dust attenuation at the bright end at all redshifts. Our results almost overlap with the relations found in Tacchella et al. (2013, 2018), Trac et al. (2015) with $\lesssim$0.3 dex differences in halo masses at all luminosities and redshifts. However, we predict a less steep relation at $z = 8$ compared with Shimizu et al. (2014). At all redshifts, we predict a much brighter UV luminosity for a given halo mass compared with the results of Endsley et al. (2019). This is likely because we include all the subhaloes (both central and satellite galaxies) identified in the simulations in our analysis, while they only included haloes (galaxy clusters) in their analysis.

Compared with the emipirical model in Tacchella et al. (2018), our predicted relation exhibits similar scatter in halo mass at the bright end while having significantly larger scatter at the faint end. In Tacchella et al. (2018), the star formation history of a galaxy is uniquely determined by the accretion history of its host halo. Haloes with the same mass may have different assembly histories and thus different amounts of stellar component. This results in scatter in scaling relations involving halo mass and galaxy properties. However, this empirical model assumed that the SFR is proportional to the gas accretion rate on to the halo, and that the star formation efficiency solely depends on the halo mass. In simulations, given the same mass accretion history of a host halo, baryonic matter can

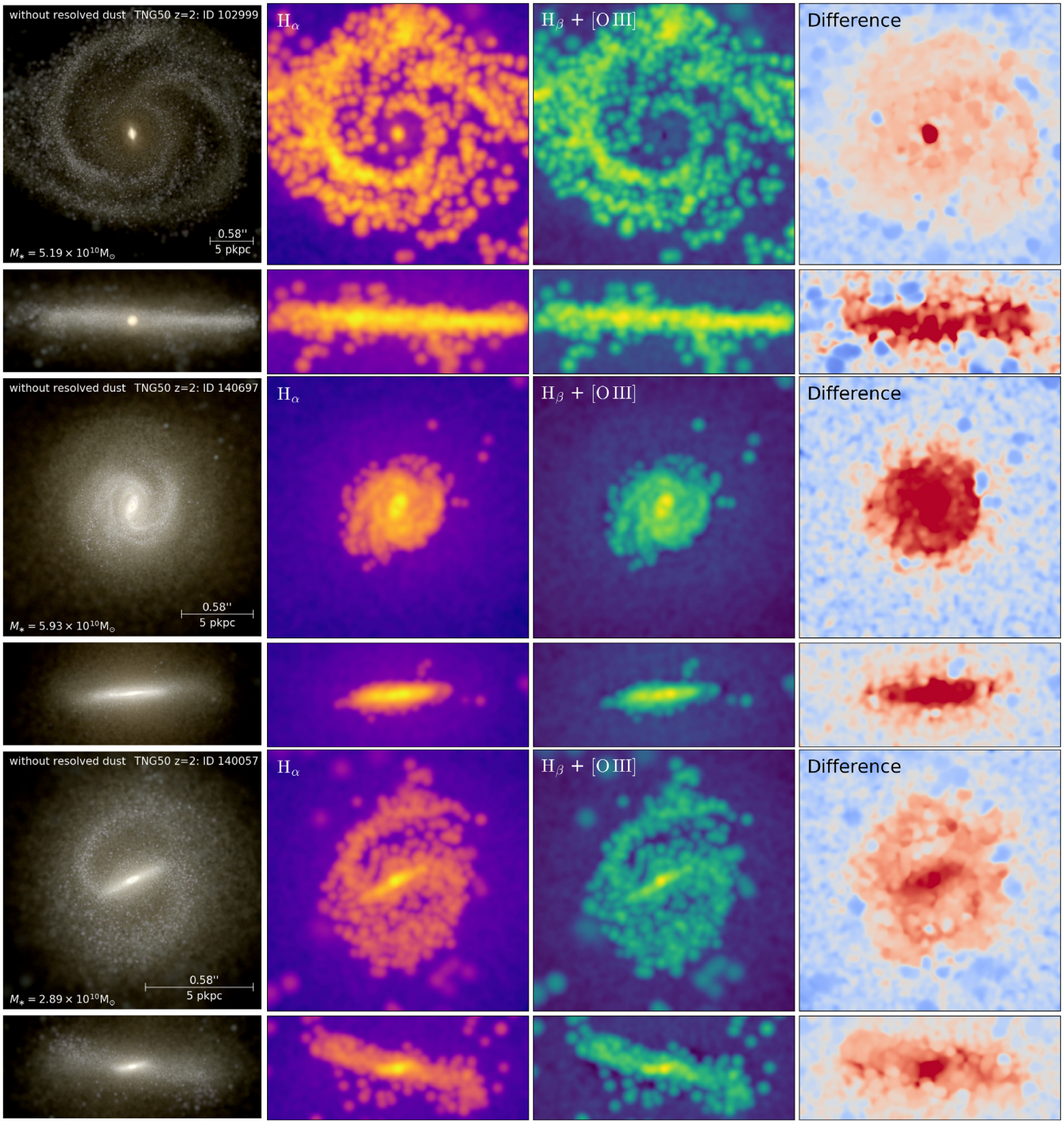

Figure 1. Face-on and edge-on images of selected TNG50 galaxies at $z = 2$. Left-hand column: *JWST* NIRCam F115W, F150W, F200W bands synthetic images (without point spread and noise); Middle left (right) column: emission line strength maps of H_α ($H\beta + [O\,III]$). The maps have been smoothed with a Gaussian kernel to alleviate artificial clumpiness. The width of the kernel is roughly the angular resolution of the *JWST* NIRCam, ∼0.03–0.06 arcsec; Right-hand column: Maps of relative differences in the emission line strength of $H\alpha$ and $H\beta + [O\,III]$, $(\log L_{H\beta+[O\,III]} - \log L_{H\alpha}) - (\log L_{H\beta+[O\,III]} - \log L_{H\alpha})_{\rm mean}$. The red regions indicate stronger $H\alpha$ emission and the blue regions indicate stronger $H\beta + [O\,III]$ emission (note that $H\alpha$ is generally stronger than $H\beta + [O\,III]$ in these galaxies, so we have already subtracted the mean difference before making this comparison). We find that $H\alpha$ is relatively stronger in the star-forming regions, e.g. spiral arms and discs, while $H\beta + [O\,III]$ is relatively stronger at the outskirts of the galaxies. Such phenomena are mainly driven by the difference in the metallicity of star-forming gas in these regions. As we will show, the difference in the spatial origins of the emission lines will have a significant impact on the dust attenuation of the lines. All the images shown here do not include the resolved dust attenuation.

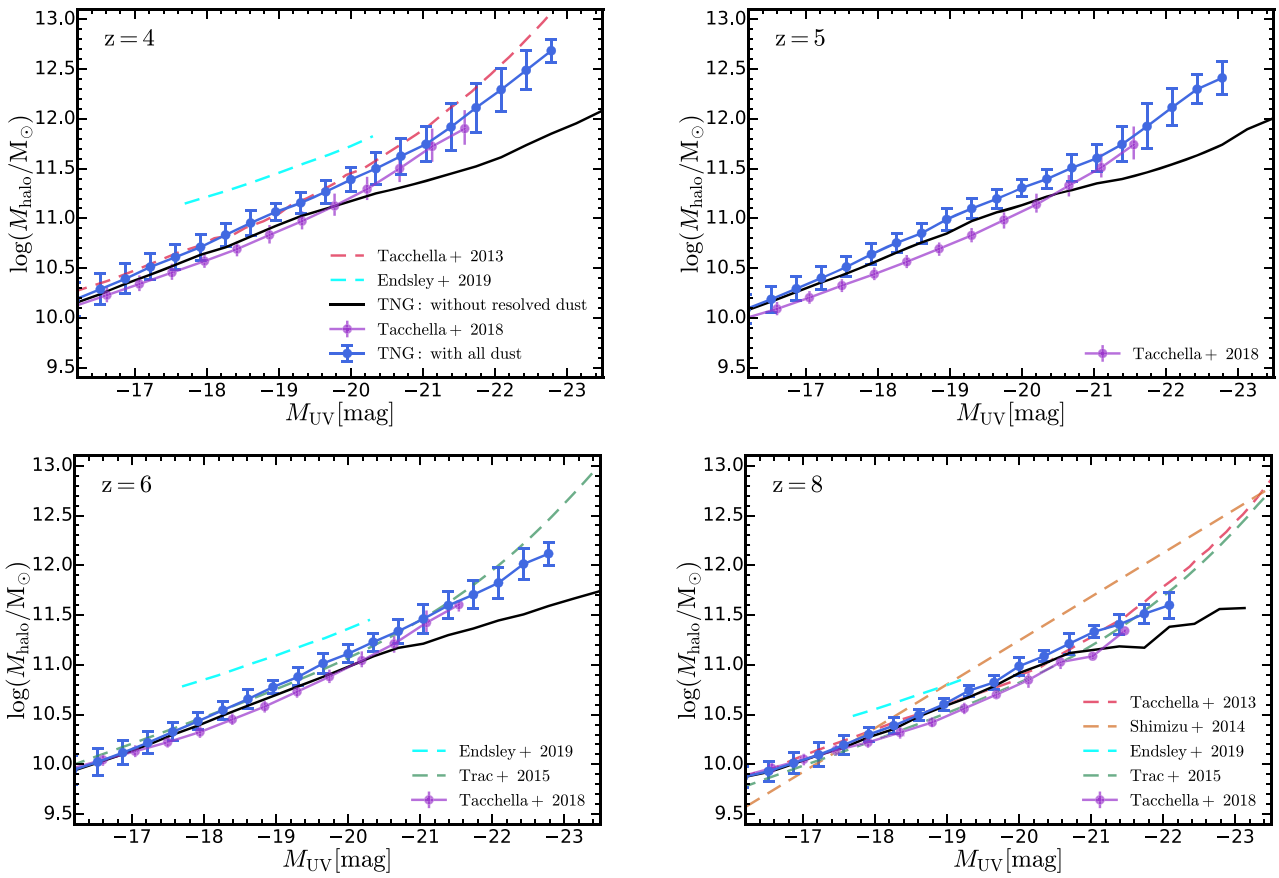

Figure 2. Galaxy host halo mass versus rest-frame UV magnitude relations at $z = 4$, 5, 6, 8 from the IllustrisTNG simulations. The blue circles and the lines show the median $\log(M_{\rm halo}/{\rm M}_\odot)$ within each dust attenuated UV magnitude bin. The error bars represent the 1σ dispersions in $\log(M_{\rm halo}/{\rm M}_\odot)$ of the samples. The black lines indicate the relations when no resolved dust attenuation is taken into account. We compare our results with the relations obtained in empirical models: Tacchella et al. (2013, the red dashed lines); Trac, Cen & Mansfield (2015, the green dashed lines); Tacchella et al. (2018, the purple lines and the circles); Endsley et al. (2019, the cyan-dashed lines). We also compare them with the prediction from the hydrodynamical simulation of Shimizu et al. (2014) shown in the orange-dashed line. Our predictions are qualitatively consistent with these studies in that the relations monotonically increase and exhibit a steepening induced by the dust attenuation at the bright end at all redshifts.

be accreted and cool down for star formation in different modes and the star formation efficiency can be affected by properties other than the halo mass, e.g. the halo concentration and the environment in which the halo resides. This results in additional scatter in the scaling relation.

5.2 Galaxy emission line luminosity functions

5.2.1 Hα luminosity function

Determining the cosmic star formation history is important for understanding galaxy formation and evolution. Numerous efforts (e.g. Duncan et al. 2014; Madau & Dickinson 2014; Salmon et al. 2015) have been made to measure the SFR density at high redshifts ($z \gtrsim 4$). Most of these works measured the SFRs of galaxies based on broad-band photometry, which suffers from caveats with respect to both completeness (e.g. Inami et al. 2017) and contamination with strong nebular emission (e.g. Schaerer & de Barros 2009; Stark et al. 2013; Wilkins et al. 2013). Nebular emission line luminosities will become a better proxy to measure the SFRs of galaxies at high redshift with the help of *JWST*. Massive, short-lived stars are direct tracers of recent star formation. The large amount of ionizing photons produced by these stars ionize surrounding gas. Hydrogen recombination cascades then produce nebular line emission, including the Balmer series lines such as Hα and Hβ as well as forbidden lines such as [O II] and [O III]. Among them, Hα is the most widely used and most sensitive star formation indicator. Compared with the UV, Hα is located at a longer wavelength and is naturally considered less affected by dust attenuation. For example, a typical value of the dust attenuation of Hα is often assumed to be $A_{\rm H\alpha} \simeq 1$ mag (Garn et al. 2010; Ibar et al. 2013; Sobral et al. 2012, 2013; Stott et al. 2013) at $z \lesssim 2$, while the attenuation in the UV at similar redshifts can easily reach $\gtrsim$2 mag in galaxies with stellar masses larger than $10^{10}\,{\rm M}_\odot$ (e.g. Heinis et al. 2014; Pannella et al. 2015; Reddy et al. 2018).

In Paper I, we have presented the Hα luminosity functions at $z = 2$, 4 and compared those with observations where we found a marginal consistency. We have also studied the scaling relation between SFR and Hα luminosity at $z = 2$ and found excellent agreement with the local calibrations (Kennicutt 1998; Murphy et al. 2011). Currently, ground-based observations can only probe the Hα luminosity function at $z \lesssim 3$. Since *JWST* will probe the Hα luminosity functions at $z \gtrsim 3$ for the first time, it is timely to make more predictions for the Hα luminosity function at high redshift with our model as a guide for future observations.

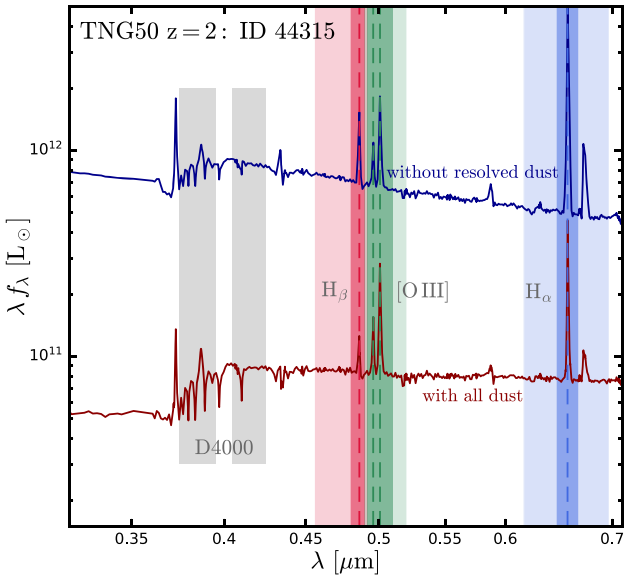

Figure 3. Constructed filters and galaxy SEDs. We show filters constructed to derive the emission line luminosities and the Balmer break at 4000 Å; (D4000). Synthetic SEDs of a star-forming galaxy in TNG50 are presented for reference. The SED with all dust attenuation (both resolved and unresolved) is shown in the red line, while the one without the resolved dust attenuation is shown in the blue line. The centres of the emission lines studied in this paper are marked by the vertical dashed lines. The shaded regions indicate the wavelength ranges covered by the filters. The lighter (darker) shaded regions correspond to broad (narrow) band filters.

Table 2. Details of the filters. The centre wavelengths and the wavelength coverages of the constructed broad-band and narrow band filters in measuring the emission line luminosities and the Balmer break at 4000 Å; (D4000). The filters are all designed to have a top-hat shape. For D4000, we only need two broad-band filters to measure the mean fluxes.

Target name	Centre wavelength	Broad-band	Narrow band
H α	6563 Å	6163–6963 Å	6463–6663 Å
H β	4861 Å	4561–4921 Å	4801–4900 Å
[O III]	4959 and 5008 Å	4900–5200 Å	4921–5100 Å
D4000+	–	4050–4250 Å	–
D4000−	–	3750–3950 Å	–

We follow the method discussed in Paper I to derive the H α luminosity of a galaxy. We first construct broad-band and narrow band top-hat filters around the emission line. The detailed information of these filters are listed in Table 2. In Fig. 3, we show all the filters constructed to derive the emission line luminosities along with the SEDs of a star-forming galaxy in TNG50. We then convolve the SED of the galaxy with these two filters and obtain the filter averaged fluxes (luminosity per unit wavelength), $f_{\rm BB}$ (broad-band) and $f_{\rm NB}$ (narrow band). We then derive the luminosity and the equivalent width (EW) of the line as (e.g. Lee et al. 2012; Sobral et al. 2013, 2015; Matthee et al. 2017)

$$L_{\rm line} = \Delta\lambda_{\rm NB}\,\frac{f_{\rm NB}-f_{\rm BB}}{1-\frac{\Delta\lambda_{\rm NB}}{\Delta\lambda_{\rm BB}}},\quad {\rm EW} = \Delta\lambda_{\rm NB}\,\frac{f_{\rm NB}-f_{\rm BB}}{f_{\rm BB}-f_{\rm NB}\frac{\Delta\lambda_{\rm NB}}{\Delta\lambda_{\rm BB}}}, \quad (2)$$

where $\Delta\lambda$ is the width of the top-hat filter. We perform this calculation for every galaxy in the simulations. Then, we perform the same resolution correction, binning, and combination procedure as in Section 5.1 in deriving the luminosity function. We also fit the predicted H α luminosity function with a Schechter function:

$$\phi(\log L) = \ln 10\ \phi_*\Big(\frac{L}{L_*}\Big)^{1+\alpha}\exp\Big(-\frac{L}{L_*}\Big), \quad (3)$$

where α is the faint-end slope, L_* is the break luminosity, and ϕ_* is the number density normalization. We will refer to this best-fitting Schechter function as the 'predicted H α luminosity function' in the following analysis. In the top left-hand panel of Fig. 4, we present the predicted H α luminosity functions at $z = 2-5$ compared with the best-fitting luminosity functions found in observations at $z \leq 2.23$ (Sobral et al. 2013). We also compare the results with the observational binned estimations at $z \simeq 2$ taken from Lee et al. (2012) and Sobral et al. (2013; denoted as L12 and S13). We scale these binned estimations that are not performed exactly at $z = 2$ to $z = 2$ using the redshift-dependent luminosity function fits in Sobral et al. (2013). We note that these studies have performed their own dust attenuation corrections, so we reintroduce the dust attenuation here based on the estimated $A_{\rm H\alpha}$s in these papers. Our prediction at $z = 2$ is ∼0.3 dex dimmer than these binned estimations at the bright end as we have already found in Paper I. We note that the unresolved dust attenuation implemented through the MAPPINGS-III SED library has been calibrated for the local Universe (Groves et al. 2008) and uncertainties arise when applying this to high-redshift galaxies. In addition, contamination from active galactic nuclei (AGN) also potentially contribute to the luminous bins in observations. For example, in Sobral et al. (2013), ∼15 per cent of the sources observed at $z = 1.47$ and 2.23 were potentially AGN. In Matthee et al. (2017), the X-ray fraction of the sources reached ∼20–50 per cent at $L_{\rm H\alpha} \sim 10^{43}$ erg s^{-1} at $z \sim 2$. Both factors could explain the discrepancy at the bright end. The H α luminosity function exhibits a strong evolution in its break luminosity from $z = 0$ to $z \simeq 2-3$. However, at $z \gtrsim 2-3$, it has only a mild evolution despite a slight decrease in the number density normalization. The evolution of the number density normalization at $z \gtrsim 2-3$ is likely following the hierarchical build-up of structure in the Universe. The sharp decline in the break luminosity at $z \lesssim 2-3$ is likely driven by the quenching of galaxies, which shuts down star formation and halts the nebular line emission associated with young stars. In the other three panels of Fig. 4, we present the evolution of the best-fitting Schechter function parameters compared with observations (Garn et al. 2010; Hayes et al. 2010; Lee et al. 2012; Sobral et al. 2013, 2015). Our best-fitting parameters at $z = 2-5$ are consistent with the evolutionary trend found at $z \lesssim 2$: the faint-end slope is stable at low redshift and becomes steeper towards higher redshift; the number density normalization is relatively stable at low redshift followed by an apparent decrease at $z \gtrsim 2-3$; the break luminosity increases rapidly at low redshift followed by mild evolution at $z \gtrsim 2-3$. We note that dust attenuation is not the primary driver for this evolutionary pattern, since such an evolutionary pattern is preserved when the resolved dust attenuation is not taken into account. However, potential underestimation of the line luminosity exists due to our inability to self-consistently model the unresolved dust component and control its strength. This would mainly affect the evolution of the break luminosity that may increase faster than predicted at $z \gtrsim 2-3$.

5.2.2 *H β + [O III] luminosity function*

Redshift $z = 2$ is about the maximum redshift that H α surveys can be performed on the ground since H α at higher redshift falls into

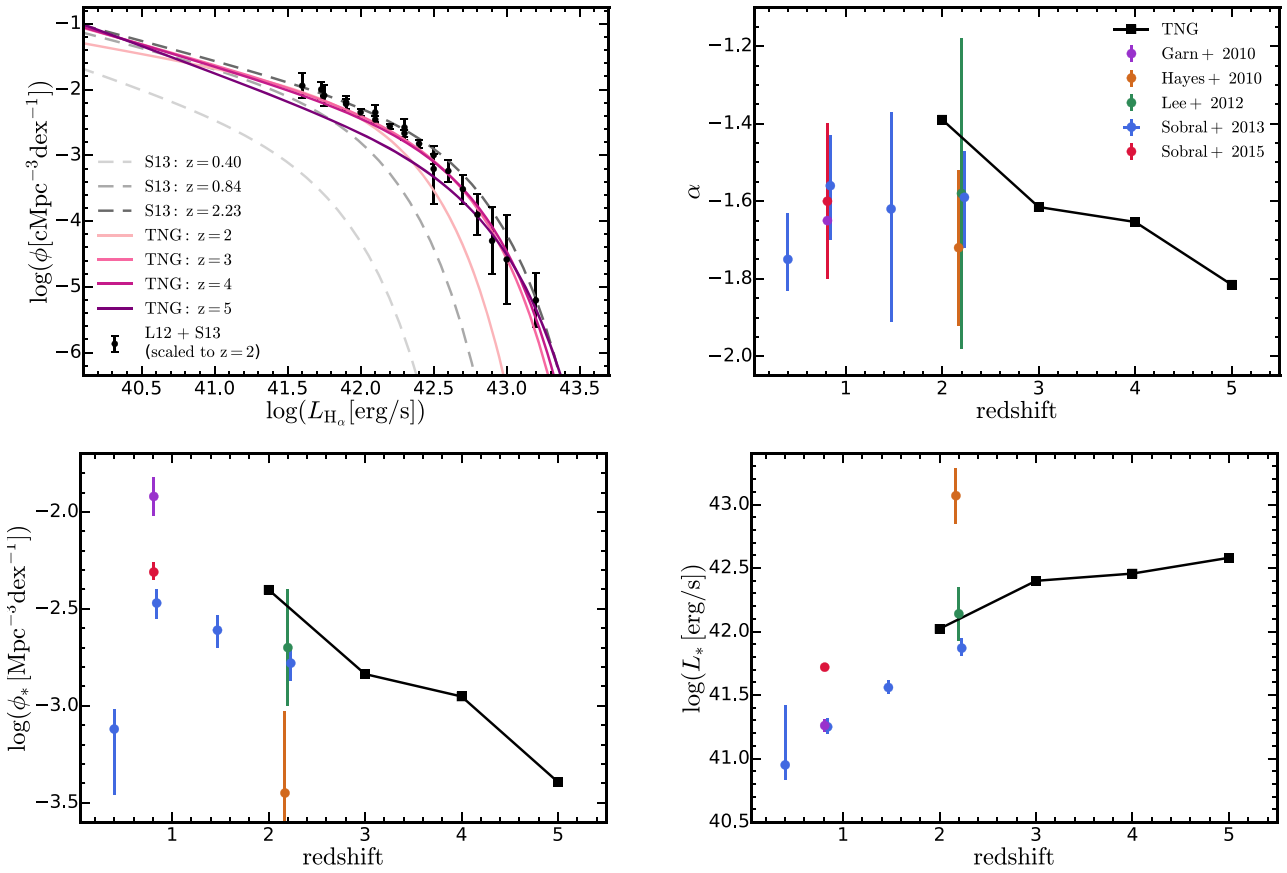

Figure 4. Evolution of the H α luminosity function from the IllustrisTNG simulations. Top left: Evolution of the H α luminosity functions at $z = 2-5$ predicted based on the IllustrisTNG simulations. Lines with the darker colours indicate luminosity functions at higher redshifts. We compare the predictions with the best-fitting luminosity functions found in observations at $z \leq 2.23$ (Sobral et al. 2013). We also compare the results with the observational binned estimations at $z \simeq 2$ taken from Lee et al. (2012) and Sobral et al. (2013; denoted as L12 and S13, respectively). We scale these binned estimations that are not performed exactly at $z = 2$ to $z = 2$ using the redshift-dependent luminosity function fits in Sobral et al. (2013). The H α luminosity function exhibits different evolutionary patterns at low and high redshift separated at $z \simeq 2-3$. Top right and bottom row: Best-fitting Schechter function parameters of the H α luminosity function. We compare our predictions with observations (Hayes, Schaerer & Östlin 2010; Garn et al. 2010; Lee et al. 2012; Sobral et al. 2013, 2015). The predicted evolution of these parameters at $z \geq 2$ is consistent with the evolutionary trend found in observations at $z \lesssim 2$. The rapid increase in the break luminosity L_* at $z \lesssim 2-3$ is followed by a decrease in the number density normalization at $z \gtrsim 2-3$.

the mid-IR and is blocked by water vapour and carbon dioxide in the atmosphere. Measurements of galaxy SFRs at higher redshift with ground-based facilities would require other emission lines as star formation indicators. For example, H β at 4861 Å; doublet at 4959 Å; 5007 Å; and O[II] at 3727 Å can be probed up to $z \sim 3-5$. Here, we explore the luminosity function of H β + O[III]. Because the H β and [O III] emission lines are close in wavelengths and are hard to distinguish from each other, their combined luminosity is usually measured in observations. Since we have accurate high-resolution SEDs of galaxies and can distinguish the two lines properly, we measure their line luminosities separately and then add them to make comparisons with observations. Following the approach used to derive the H α luminosity, we construct broad-band and narrow band top-hat filters around the H β and [O III] emission lines, respectively. The detailed properties of these filters are also listed in Table 2.

In the top two panels of Fig. 5, we compare the predicted H β + [O III] luminosity functions at $z = 2$ with observations at $z = 2.2$ (Khostovan et al. 2015) and compare the luminosity function at $z = 3$ with observations at $z = 3.2$ (Khostovan et al. 2015; Matthee et al. 2017). We find that the predicted H β + [O III] luminosity functions are in good agreement with observations at both redshifts. The differences in luminosities are $\lesssim$0.1 dex, except for one binned value at the bright end at $z \simeq 3$ that could be affected by contamination. For the green-shaded regions in the figures, the vertical boundaries indicate the detection limits of a possible observational campaign, assuming a target SNR = 10 and an exposure time $T_{\rm exp} = 10^4$ s, using the *JWST* NIRSpec instrument. The detection limits are also listed in Table 4. The horizontal boundaries indicate a reference number density that corresponds to one galaxy per dex of luminosity in an effective field of view 9.2 arcmin^2 with a survey depth $\Delta z = 1$. The calculations for the detection limits and the introduction of the field of view of a possible observational campaign carried out by the *JWST* NIRSpec instrument are discussed in Section 5.2.4. The numbers labelled are the numbers of galaxies expected to be observed by a survey of depth $\Delta z = 1$ using the *JWST* NIRSpec instrument (under the assumed observation setup). In the bottom left-hand panel of Fig. 5, we present the predicted H β + [O III] luminosity function at $z = 8$, which has never been reached by any direct survey. Recently, De Barros et al. (2019) presented the first constraint on the H β + [O III] luminosity function at $z \sim 8$. They measured the H β + [O III] line luminosities and the

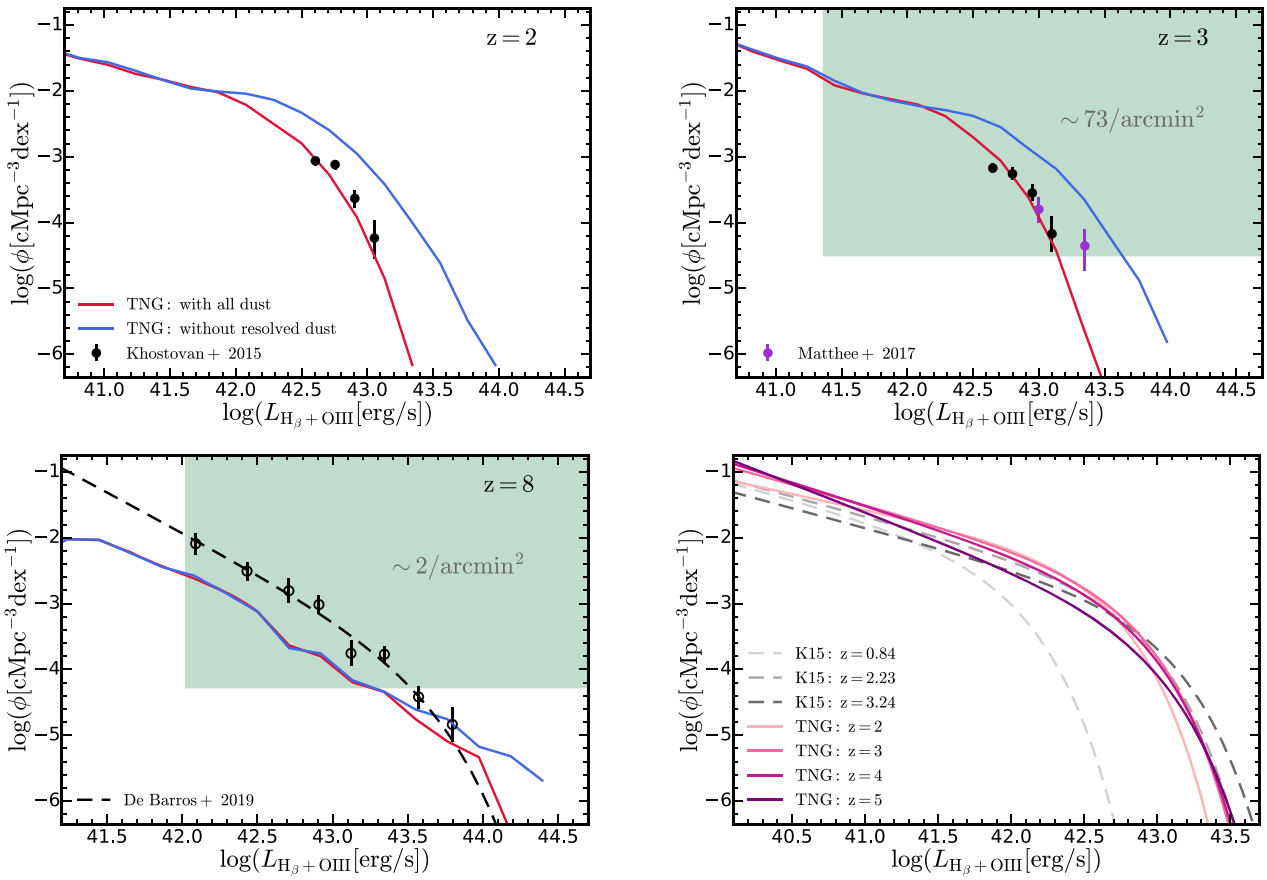

Figure 5. Evolution of the H β + [O III] luminosity function from the IllustrisTNG simulations. Top row and bottom left: Predicted H β + [O III] luminosity functions at $z = 2, 3, 8$. The blue lines show the luminosity functions when no resolved dust attenuation is taken into account. The red lines show the luminosity functions with all dust attenuation. We compare our results with observations from Khostovan et al. (2015) and Matthee et al. (2017) at $z = 2.2$ and 3.2, respectively. Our predictions are in good agreement with these observations. For the $z = 8$ case, we compare our luminosity function with a recent indirect measurement from De Barros et al. (2019). Their best-fitting Schechter function is shown in the black-dashed line. Their estimates based on individual UV luminosity function data points are shown in the open circles. We find marginal consistency at the bright end despite our prediction being ∼0.5 dex lower than their results at $L \lesssim 43.5\,\mathrm{erg\,s^{-1}}$. For the green-shaded regions, the vertical boundaries indicate the detection limits of a possible observational campaign, assuming a target SNR = 10 and an exposure time $T_{\mathrm{exp}} = 10^4$ s, using the *JWST* NIRSpec instrument. The horizontal boundaries indicate a reference number density corresponding to one galaxy per dex of luminosity in an effective field of view 9.2 arcmin^2 with a survey depth $\Delta z = 1$. The numbers labelled are the numbers of galaxies expected to be observed by a survey of depth $\Delta z = 1$ using the *JWST* NIRSpec instrument (under the assumed observation setup). Bottom right: Evolution of the H β + [O III] luminosity function at $z = 2$–5. The lines with darker colours indicate luminosity functions at higher redshifts. We compare our predicted luminosity functions with observations at lower redshift ($z \leq 3.24$) from Khostovan et al. (2015). The evolutionary pattern of the H β + [O III] luminosity function is similar to that of the H α luminosity function.

UV luminosities of ∼100 Lyman Break galaxies at $z \sim 8$. They fitted a $L_{\mathrm{H}\beta+\mathrm{O[III]}}$–$M_{\mathrm{UV}}$ scaling relation and then convolved the well-measured galaxy rest-frame UV luminosity function with this relation to derive the H β + [O III] luminosity function. We compare our result with their best-fitting Schechter function and the individual data points convolved from the rest-frame UV luminosity function binned estimations. We find marginal consistency at the bright end despite our prediction being ∼0.5 dex lower than their result at $L < 43.5\,\mathrm{erg\,s^{-1}}$. This is roughly consistent with our prediction for the galaxy rest-frame UV luminosity function at $z = 8$, which is also slightly lower than observations. We fit the predicted H β + [O III] luminosity functions with a Schechter function. In the bottom right-hand panel of Fig. 5, we present the evolution of the predicted H β + [O III] luminosity functions at $z = 2$–5. We compare our best-fitting Schechter functions with observations by Khostovan et al. (2015) at $z \leq 3$. We find a similar evolutionary pattern to the H α luminosity function in that the break luminosity is evolving rapidly at low redshift followed by a mild decrease in the number density normalization towards $z \gtrsim 2$–3.

5.2.3 *Differential attenuation of emission lines*

In many studies, dust attenuation of emission lines has been assumed to follow the attenuation curve of the continuum emission. Following this assumption, the attenuation of emission lines at long wavelengths is naturally thought to be limited. However, as shown in Fig. 6, the resolved dust attenuation of H α, which is located at 6563 Å, is surprisingly stronger than that of H β + [O III], which is located at around 5000 Å. This is in contradiction with the prediction from the attenuation curve of the continuum that the attenuation at lower wavelengths is stronger. The H α line is indeed less attenuated than the UV but is more heavily attenuated than expected from the attenuation curve of the continuum. This phenomenon is also illustrated in Section 5.5 and Fig. 13 where spikes appear in the

Table 3. Detection limits of a possible observational campaign (under the assumed set-up) using the *JWST* NIRCam slitless spectroscopy. R is the nominal resolving power and S is the continuum sensitivity. Here, we take the sensitivity of the Module A long-wavelength grism. Detection limits of the line luminosites were calculated by Greene et al. (2017) assuming a target SNR = 10 and an exposure time $T_{\rm exp} = 10^4$ s.

Filter	R	$\lambda_{\rm obs}(\mu{\rm m})$	Target line and redshift	Detection limit (SNR = 10, $T_{\rm exp} = 10^4$ s)		
				S(nJy)	$L_{{\rm H}\alpha}({\rm erg\,s^{-1}})$	$L_{{\rm H}\beta+[{\rm O\,III}]}({\rm erg\,s^{-1}})$
F322W2	∼1500	∼2.5	Hα at $z = 3$; Hβ + [O III] at $z = 4$	∼9100	41.90	42.19
F444W	∼1500	∼4	Hα at $z = 5$; Hβ + [O III] at $z = 7$	∼7800	42.04	42.38
F444W	∼1500	∼4.5	Hα at $z = 6$; Hβ + [O III] at $z = 8$	∼10 000	42.30	42.59

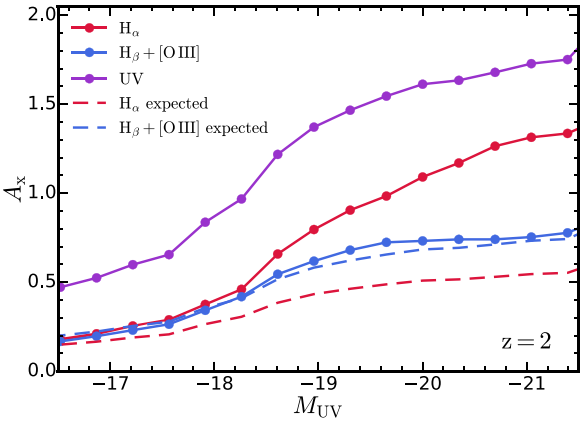

Figure 6. Resolved dust attenuation of galaxy UV and emission line luminosities versus rest-frame UV magnitude at $z = 2$ from the IllustrisTNG simulations. The dashed lines represent the expected attenuation of the lines from $A_{\rm UV}$ assuming the canonical Calzetti attenuation curve. The resolved dust attenuation of Hα, which is located at 6563 Å, surprisingly is stronger than that of Hβ + [O III], which is located at around 5000 Å. This is in contradiction with the prediction from the attenuation curve of the continuum that the attenuation at lower wavelength is stronger. The Hα line is more heavily attenuated than expected from the attenuation curve of the continuum. These phenomena demonstrate the differential attenuation of emission lines.

radiative transfer based attenuation curves where emission lines are located. We note that the dust attenuation we compare to here is the resolved dust attenuation. So, the differential attenuation found here is not caused by the unresolved dust attenuation in our modelling of young stellar populations. If we also take the unresolved dust attenuation into account, the preferential attenuation of emission lines will be even stronger.

We attribute the differential attenuation of emission lines to dust geometry (the geometrical and spatial distribution dust with respect to radiation sources). In Fig. 7, we present the *JWST* bands synthetic images (with and without dust attenuation), the resolved dust mass distribution and the Hα emission strength map of a TNG50 galaxy at $z = 2$. As shown in the right-hand column of Fig. 7, the spatial distribution of the resolved dust and the emission line strength are well correlated. Since we have assumed that dust is traced by metals in cold, star-forming gas in our post-processing procedure, dust naturally concentrates in star-forming regions where the nebular line emission originates. Therefore, the column density of dust is relatively larger for line emission than the continuum emission, which is distributed more evenly in the galaxy. This results in the differential attenuation of emission lines. Furthermore, as illustrated in Fig. 1, the spatial origin of Hα and Hβ + [O III] are different in galaxies at $z = 2$. The Hα emission is stronger in star-forming regions, e.g. spiral arms and discs, where metallicity is high and dust is abundant. The Hβ + [O III] emission is stronger in the outskirts of the galaxies where metallicity is low and the regions are dust-poor. As a consequence of these differences, the sources of Hα are more obscured by dust than those of Hβ + [O III], which explains the inverse hierarchy of the resolved dust attenuation of Hβ + [O III] and Hα. In observations, there is evidence for this differential attenuation of emission lines. For example, in Reddy et al. (2015), the colour excess of ionized gas was found to be larger than that of stellar continuum. The difference in the attenuation of Hα and the continuum showed a positive correlation with galaxy SFR.

5.2.4 JWST *forecast*

JWST is going to provide the first spectroscopic access to optical emission lines of high-redshift galaxies (e.g. Greene et al. 2017; Chevallard et al. 2019; De Barros et al. 2019). For example, the *JWST* NIRCam can perform imaging or slitless spectroscopy in either of the two 2.2 × 2.2 arcmin^2 fields of view (Gardner et al. 2006). A wide-field high-redshift survey of Hα (Hβ and [O III]) can be performed at $z \sim 2.7$−6.6 ($z \sim 3.8$−9.0; Greene et al. 2017). The detection limits of a possible observational campaign using this technique are listed in Table 3. In addition, the NIRSpec instrument on *JWST* offers multi-object spectroscopy covering a large wavelength range from 0.6 to 5.3μm with resolving power up to $R \sim 2700$ (Gardner et al. 2006). It enables the detection of Hα (Hβ and [O III]) up to $z = 7$ ($z = 9$). When operating with four quadrants, each of which covers 2.3 arcmin^2, NIRSpec will cover an effective field of view of 9.2 arcmin^2. The sensitivity of the NIRSpec technique can be calculated with the *JWST* Exposure Time Calculator[7] (ETC; Pontoppidan et al. 2016).

Here, we provide two example calculations of the detection limits of the emission line luminosities under different assumptions. For the first case, we assume that the target emission line is well resolved and the continuum around it is detected with a desired SNR. The online documentation[8] (STScI 2018) of the NIRSpec expected performance provides a calculation of the wavelength-dependent limiting flux sensitivity with a target SNR = 10 and an exposure time $T_{\rm exp} = 10^4$ s (see the documentation for the detailed parameter set-up). We then take the limiting flux sensitivity, $S_\nu^{\rm lim}$, where the emission lines are located. In this case, $S_\nu^{\rm lim}$ represents the detection limit of the continuum around the lines. We convert it to the detection limit of the line luminosity as

$$L_{\rm line}^{\rm lim} = 4\pi\, D_{\rm L}(z)^2 \frac{\rm c}{\lambda_{\rm obs}^2} S_\nu^{\rm lim}\, {\rm EW}, \quad (4)$$

[7] https://jwst.etc.stsci.edu/

[8] https://jwst-docs.stsci.edu/near-infrared-spectrograph/nirspec-predicted-performance/nirspec-sensitivity

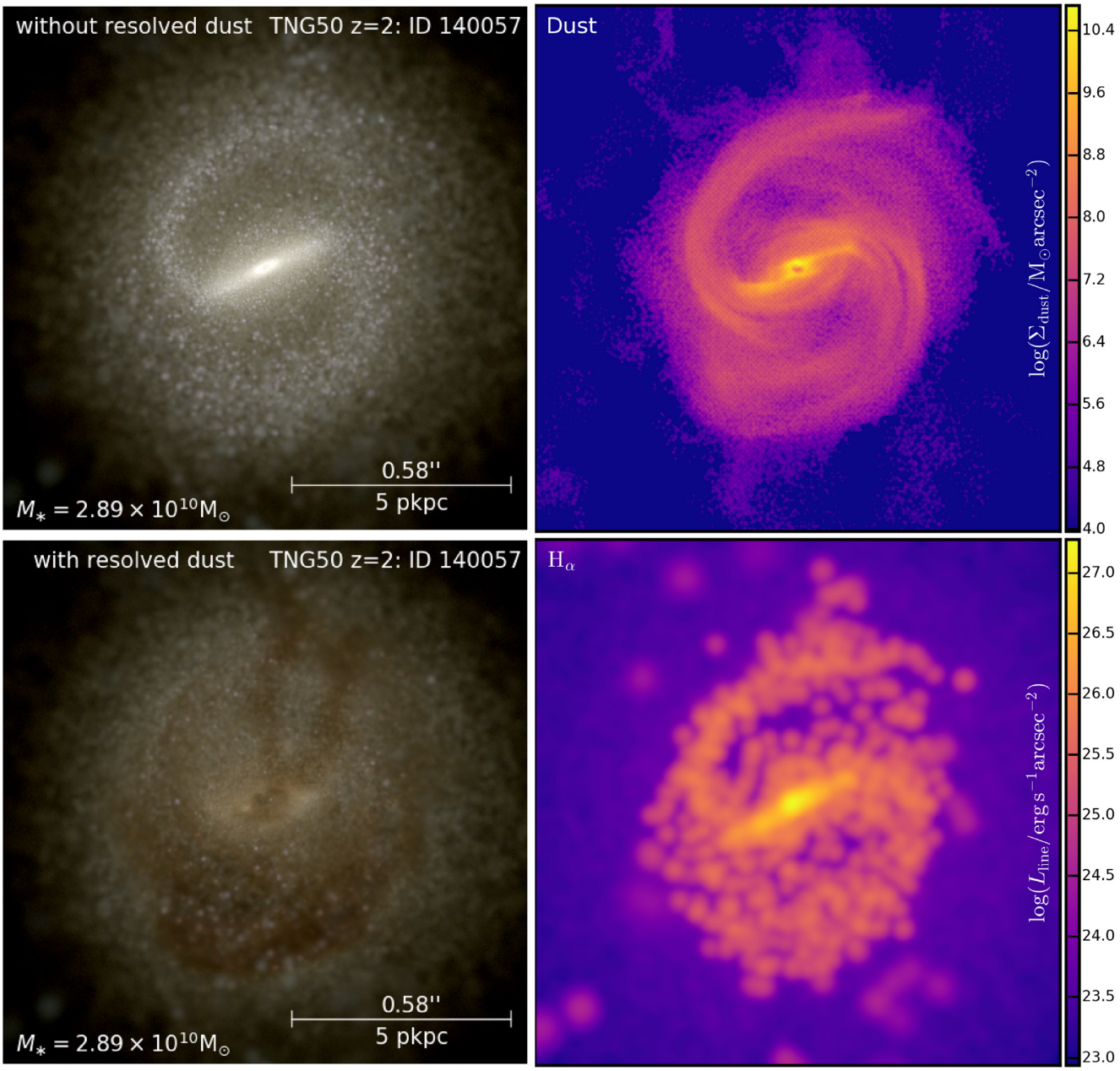

Figure 7. Images of a TNG50 galaxy at $z = 2$. Top left: *JWST* NIRCam F115W, F150W, F200W bands synthetic images without the resolved dust; Bottom left: *JWST* NIRCam F115W, F150W, F200W bands synthetic image with all dust, assuming the dust-to-metal ratio to be 0.9; Top right: resolved dust mass distribution with warmer colour indicating higher dust mass density; Bottom right: Hα emission line strength map. It is smoothed in the same way as the maps in Fig. 1. The images demonstrate that the origins of line emission are spatially correlated with the resolved dust distribution, which would result in the differential attenuation of emission lines.

where $\lambda_{\rm obs}$ is the observed wavelength of the line, $D_{\rm L}(z)$ is the luminosity distance of an object at redshift z, and EW is the EW of the line, assumed to be 100 Å, here. At this line luminosity limit, the lines with EW below the assumed value can be detected. For the second case, we assume that the continuum cannot be properly detected and the emission lines are not completely resolved. The continuum flux in this case is subdominant with respect to the noise so we can ignore it. Using the *JWST* ETC, assuming the lines have width $\sim$150 km s^{-1} and no continuum contribution, we calculate the detection limits of line luminosities with a target SNR = 10 and an exposure time $T_{\rm exp} = 10^4$ s. We adopt 10 groups per integration, 24 integrations per exposure and one exposure per specification to achieve the total exposure time 10^4 s. The read-out pattern is chosen to be NRS. The background configuration is assumed to be the same as in Paper I and the source is assumed to be a point source. The calculated detection limits with the two approaches as well as the details of the JWST NIRSpec dispersers and filters are all listed in Table 4. We note that the detection limits we use for related predictions in this paper are calculated using the second approach.

Table 4. Detection limits of a possible observational campaign (under the assumed set-up) using the *JWST* NIRSpec instrument. R is the nominal resolving power and S is the continuum sensitivity. Detection limits of the line luminosites are calculated assuming a target SNR = 10 and an exposure time $T_{\rm exp} = 10^4$ s. We present the calculated results with the two approaches (see Section 5.2.4) labelled by numbers. The first approach assumes the continuum around the line is detected, while the second approach does not. We note that the detection limits we use for related predictions in this paper are calculated using the second approach. Characteristics of the dispersers and filters are also presented.

Disperser and filter [λ coverage (μm)]	R	$\lambda_{\rm obs}$ (μm)	Target line and redshift	Detection limit (SNR = 10, $T_{\rm exp} = 10^4$ s) S(nJy)	$L_{\rm H\alpha}$(erg s^{-1})	$L_{\rm H\beta+[O\,III]}$(erg s^{-1})
G235M/F170LP	∼1000	∼2	Hα at $z = 2$; Hβ + [O III] at $z = 3$	∼1100	①41.41 ②40.93	①41.82 ②41.36
(1.66-3.07)		∼2.5	Hα at $z = 3$; Hβ + [O III] at $z = 4$	∼1200	①41.63 ②41.23	①41.97 ②41.53
G395M/F290LP	∼1,000	∼4	Hα at $z = 5$; Hβ + [O III] at $z = 7$	∼1100	①41.76 ②41.50	①42.09 ②41.84
(2.87-5.10)		∼4.5	Hα at $z = 6$; Hβ + [O III] at $z = 8$	∼1500	①41.95 ②41.73	①42.25 ②42.02
G235H/F170LP	∼2,700	∼2	Hα at $z = 2$; Hβ + [O III] at $z = 3$	∼3000	①41.85 ②41.11	①42.26 ②41.54
(1.66-3.05)		∼2.5	Hα at $z = 3$; Hβ + [O III] at $z = 4$	∼3300	①42.07 ②41.45	①42.41 ②41.75
G395H/F290LP	∼2,700	∼4	Hα at $z = 5$; Hβ + [O III] at $z = 7$	∼3000	①42.20 ②41.74	①42.52 ②42.08
(2.87-5.14)		∼4.5	Hα at $z = 6$; Hβ + [O III] at $z = 8$	∼4000	①42.38 ②42.00	①42.68 ②42.28

5.3 Balmer break at 4000 Å

In addition to the emission line luminosities, another important spectral feature as a star formation indicator is the Balmer break at ∼4000 Å, often referred to as D4000. In old stellar populations, opacity due to several ions in the stellar atmosphere induces a discontinuity in the flux around 4000 Å. This spectral feature is missing in young stellar populations. Therefore, the strength of the discontinuity around 4000 Å can be used to measure the contribution of young stellar populations to the galaxy's total emission and equivalently the specific SFR (sSFR). D4000 is usually defined as the ratio between the averaged flux in 4050−4250 Å and that in 3750−3950 Å (Bruzual A. 1983). Unlike the emission lines we studied above, measurements of D4000 do not require very high-quality spectra and are less affected by dust attenuation. It is therefore suitable for the study of star formation in galaxies at high redshift. D4000 has been used in the study of the star formation history of galaxies as well as the selection of star-forming galaxies (e.g. Kauffmann et al. 2003; Brinchmann et al. 2004; Kriek et al. 2011; Johnston et al. 2015; Haines et al. 2017). However, a direct survey of the D4000s of galaxies at high redshift ($z \geq 2$) is still lacking.

To calculate D4000, we construct two top-hat filters to measure the averaged flux (luminosity per unit wavelength) in the wavelength range 4050−4250 Å and 3750−3950 Å, respectively. These two filters are also listed in Table 2. The filters are also visualized in Fig. 3 along with the SEDs of a star-forming galaxy in TNG50. D4000 is then calculated as the ratio between the flux measured in 4050−4250 Å and that measured in 3750−3950 Å.

In Fig. 8, we present the predicted D4000 versus sSFR relation at $z = 2$. The relation combined from TNG50, TNG100, and TNG300 and its dispersion are presented with the blue line and the circles. We also show the distribution of galaxies from TNG100 with a colour mesh. The darker colour indicates more galaxies in the grid. The dust attenuation has only a limited impact on the D4000 values ($\lesssim$0.05), so we only show the D4000s of the dust attenuated SEDs here. The distribution pattern is similar for galaxies in TNG50/100/300, so we choose TNG100 galaxies as examples here. In the simulations, D4000 shows a tight correlation with sSFR at $z = 2$. The predicted relation almost overlaps with the local calibration (Brinchmann et al. 2004) at the high sSFR end. A cluster of star-forming galaxies clearly shows up at the high sSFR end followed by a tail of passive galaxies. The pattern is quite different from the bimodal distribution found in the local Universe (e.g. Kauffmann et al. 2003; Brinchmann et al. 2004). The D4000s of galaxies at $z = 2$ are systematically lower

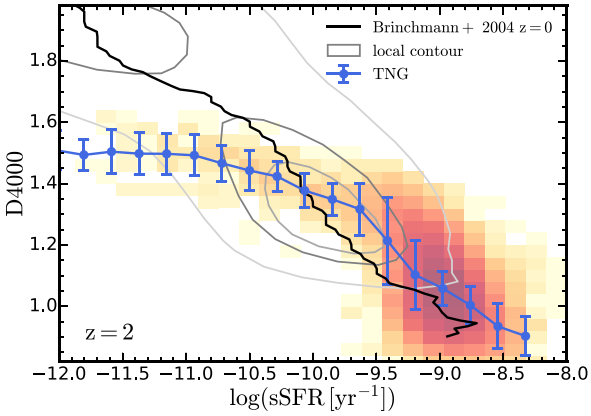

Figure 8. D4000 versus sSFR relation at $z = 2$ from the IllustrisTNG simulations. The median relation along with 1σ dispersion are shown in the blue line and the circles with the error bars. The median relation and its scatter are combined results from TNG50, TNG100, and TNG300. We also present the distribution of galaxies from TNG100 with a colour mesh. The darker colour indicates a larger number of galaxies in the grid. We compare our results with the calibration in the local Universe (Brinchmann et al. 2004) shown in the black solid line. The distribution of the observed galaxies in the local Universe is shown with the grey contours.

than those in the local Universe, while the sSFRs are systematically higher. This is consistent with the trend found at $z \lesssim 1$ (Haines et al. 2017) that the sSFRs of massive blue cloud galaxies decline steadily with time and their D4000s rise correspondingly. Another interesting fact is that, at the low sSFR end, the tail of passive galaxies at $z = 2$ does not sit on the local calibration. At fixed sSFR, the D4000s of the passive galaxies at $z = 2$ are smaller than those of the passive galaxies in the local Universe. D4000 traces the age of the stellar population. The passive galaxies at $z = 2$ were quenched relatively recently and are quite young by the time. The passive galaxies at $z = 0$ are overall older than those early-quenched galaxies and therefore exhibit higher values of D4000s.

5.4 UV continuum slope β

Calzetti, Kinney & Storchi-Bergmann (1994) parametrized the UV colour of galaxies through the UV continuum slope β defined as $f_\lambda \sim \lambda^\beta$, which can be measured from galaxy spectra or multiband photometry. Meurer et al. (1997) and Meurer, Heckman & Calzetti (1999) found a correlation between galaxy far-IR dust emission

excess and β, the IRX-β relation, and thus established β as a dust attenuation indicator (see Schulz et al. 2020, a study of this relation based on the IllustrisTNG). Such a correlation was found to exist up to $z \sim 5$ (e.g. Seibert, Heckman & Meurer 2002; Overzier et al. 2011; Reddy et al. 2012; Koprowski et al. 2018). Due to accessibility, the UV continuum slope β acts as one of the best and widely used dust attenuation indicators in the study of high-redshift galaxies. As a result, a large amount of work has been devoted to determining the distribution of β and its dependence on galaxy luminosity at different redshifts (e.g. Meurer et al. 1999; Adelberger & Steidel 2000; Ouchi et al. 2004; Papovich et al. 2004; Hathi, Malhotra & Rhoads 2008). In particular, a relation between β and galaxy rest-frame UV luminosity, or equivalently $M_{\rm UV}$, has been revealed and investigated in many studies (e.g. Bouwens et al. 2009; Finkelstein et al. 2012; Dunlop et al. 2013; Bouwens et al. 2012, 2014). The relation has enabled an empirical estimation of dust attenuation solely based on the galaxy rest-frame UV luminosity.

In practice, the UV continuum slope β is measured by performing a $f_\lambda \sim \lambda^\beta$ power-law fit on either photometric data (e.g. Bouwens et al. 2009, 2012, 2014) or SED synthesized based on photometric data (e.g. Finkelstein et al. 2012). Since we have an accurate galaxy UV SED and do not rely on photometric measurements to obtain the flux, as our fiducial method, we perform a power-law fit on the galaxy UV SED from 1450 to 3000 Å to derive β. The wavelength range is selected to cover 1450−1550 Å, where we measured the rest-frame UV luminosity and to avoid the influence of the UV bump feature of the dust attenuation curve at ∼2175 Å on the measurement of β. To test the robustness of this method, we try alternative ways to measure the UV continuum slope: varying the maximum wavelength to 2500 and 2000 Å, or calculating the slope purely with the fluxes at the head and the end of the wavelength range. We present a comparison between the results derived with different methods at the end of this section.

In Fig. 9, we compare the predicted β versus $M_{\rm UV}$ relations with recent observations (Bouwens et al. 2012; Finkelstein et al. 2012; Dunlop et al. 2013; Bouwens et al. 2014). We note that here we select only star-forming galaxies with $\log({\rm sSFR/yr^{-1}}) > -9.0$. This criterion is roughly 0.5 dex below the star formation main sequence measured at $z \simeq 2-6$ (e.g. Salmon et al. 2015; Tomczak et al. 2016; Santini et al. 2017). The $\Delta \log {\rm sSFR} > -0.5$ criterion has been demonstrated to be consistent with the *UVJ*-diagram selection adopted in observations (Fang et al. 2018; Donnari et al. 2019; Pillepich et al. 2019). At $z \gtrsim 2$, the main-sequence sSFR is slightly lower at the massive end (e.g. Tomczak et al. 2016). So, we also explore varying this selection criterion to −9.5, but we find that our results are not significantly affected. When the resolved dust attenuation is not taken into account (referred to as 'intrinsic'), β remains a constant value ∼−2.1 to 2.3 that is independent of galaxy rest-frame UV luminosities and becomes lower at higher redshift where stellar populations are younger. At the same redshift, the stellar populations of star-forming galaxies have similar ages (the sSFRs and mass doubling time scales of galaxies are similar), which results in 'intrinsic' βs almost independent of galaxy luminosities. However, the dust attenuated β shows a clear dependence on galaxy UV luminosity, with shallower slope at higher UV luminosity. This indicates that dust attenuation is stronger in galaxies with higher UV luminosity and thus makes the UV continuum shallower. Compared with observations, the $\beta - M_{\rm UV}$ relation in the simulations is not as steep as that found by Bouwens et al. (2014) at the bright end. The discrepancy is more apparent towards higher redshifts indicating a deficiency of galaxies with high β in the simulations.

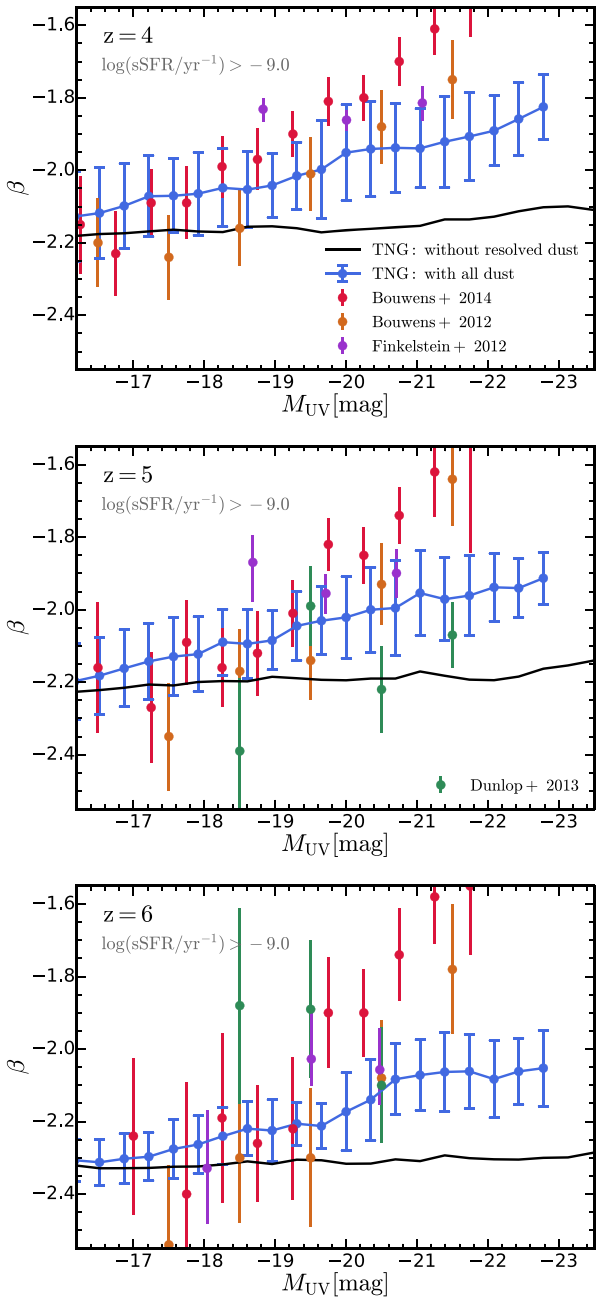

Figure 9. Predicted UV continuum slope β versus $M_{\rm UV}$ relations at $z = 4-6$ from the IllustrisTNG simulations. Here, we select only star-forming galaxies with $\log({\rm sSFR/yr^{-1}}) > -9.0$. The blue circles with the error bars and the blue lines represent relations with all dust attenuation and 1σ dispersion. The black lines show relations when the resolved dust attenuation is not taken into account. We compare them with observations from Bouwens et al. (2012), Finkelstein et al. (2012), Dunlop et al. (2013), and Bouwens et al. (2014). The predictions are consistent with observations at the faint end. At the bright end, the predicted relation is lower than observations and the slope of the predicted relation is apparently flatter. The underprediction of β is related with the deficiency in heavily attenuated galaxies at the massive end as shown in Fig. 10.

As discussed, the relationship between galaxy FIR excess (IRX) and β established β as a dust attenuation indicator. By definition, we have

$$\mathrm{IRX} = \frac{L_{\mathrm{IR}}}{L_{\mathrm{UV}}} = B\frac{L_{\mathrm{UV}}^{\mathrm{absorbed}}}{L_{\mathrm{UV}}^{\mathrm{dust}}} = B\frac{L_{\mathrm{UV}}^{\mathrm{nodust}} - L_{\mathrm{UV}}^{\mathrm{dust}}}{L_{\mathrm{UV}}^{\mathrm{dust}}} = B(10^{0.4A_{\mathrm{UV}}} - 1), \quad (5)$$

where B is a constant correction factor describing how much the far-IR luminosity can represent the total amount of energy emitted by dust and how much the dust absorption in the UV can represent the total amount of energy absorbed by dust. The typical value for this constant is 1.66−2.08 (e.g. Meurer et al. 1999; McLure et al. 2018). Therefore, IRX has a direct connection with the attenuation in the UV. The IRX versus β relation can be translated to the A_{UV} versus β relation and vice versa. The $A_{\mathrm{UV}}-\beta$ relation is often parametrized linearly as $A_{\mathrm{UV}} = k\beta + C$. However, this observational relation has a large scatter, ∼1 dex, and no consensus has been reached on parameter choices for this relation at high redshift. In the simulations, we find that the resolution corrected relations from TNG100, TNG300 do not overlap either with each other or with the relation derived from TNG50. This indicates that there are other galaxy properties that affect the $A_{\mathrm{UV}}-\beta$ relation and such galaxy properties are different in galaxies selected from TNG50/100/300. The phenomenon is consistent with the findings in observations that galaxies of different types lie differently on the IRX-β or $A_{\mathrm{UV}}-\beta$ plane. A simple and straightforward candidate for this controlling property would be the stellar mass since there is a well-established relation between A_{UV} and stellar mass (e.g. Pannella et al. 2009; Reddy et al. 2010; Buat et al. 2012; Heinis et al. 2014; Pannella et al. 2015; Álvarez-Márquez et al. 2019), which is even tighter than the $A_{\mathrm{UV}}-\beta$ relation. Recently, Álvarez-Márquez et al. (2019) even proposed a new relation combining β and stellar mass as the dust attenuation proxy. In Fig. 10, we predict the $A_{\mathrm{UV}}-M_*$ relations at $z = 2-4$ compared with observations from Heinis et al. (2014), Pannella et al. (2015), Álvarez-Márquez et al. (2016), Bourne et al. (2017), Koprowski et al. (2018), McLure et al. (2018), and Reddy et al. (2018). Here, we have also restricted our analysis to star-forming galaxies with $\log(\mathrm{sSFR/yr^{-1}}) > -9.0$ and rest-frame UV magnitude $M_{\mathrm{UV}} < -17$. Again, we find the results here not affected by varying the selection criterion for sSFR. We note that the A_{UV} presented is the resolved dust attenuation and the unresolved dust attenuation is subdominant in affecting broad-band photometry. In the simulations, there is a tight relation between A_{UV} and stellar mass. The relation is approximately linear on the $A_{\mathrm{UV}}-\log M_*$ plane when $\log(M_*/\mathrm{M}_\odot) \in [9, 11]$. The relation becomes flatter towards the low-mass end, which is consistent with the findings in McLure et al. (2018). We predict consistent results with existing observations at the low-mass end, but underpredict the attenuation at the massive end. The discrepancy is more apparent at higher redshift and could reach ∼1 mag at the massive end at $z = 4$. This is consistent with what we have found in the β versus M_{UV} relation that there is a deficiency of heavily attenuated, UV red galaxies in the simulations at the massive (bright) end.

Acknowledging the influence of stellar mass on the UV attenuation, we next study the $A_{\mathrm{UV}}-\beta$ relation at fixed stellar masses. For each simulation, we divide galaxies into three stellar mass bins, $\log(M_*/\mathrm{M}_\odot) \in [7.5, 9.0]$, $[9.0, 10.5]$, $[10.5, 12]$, and calculate the $A_{\mathrm{UV}}-\beta$ relation in each stellar mass bin, respectively. Here, we have also restricted our analysis to star-forming galaxies with $\log(\mathrm{sSFR/yr^{-1}}) > -9.0$ and rest-frame UV magnitude $M_{\mathrm{UV}} < -17$. In Fig. 11, we present the median $A_{\mathrm{UV}}-\beta$ relation with

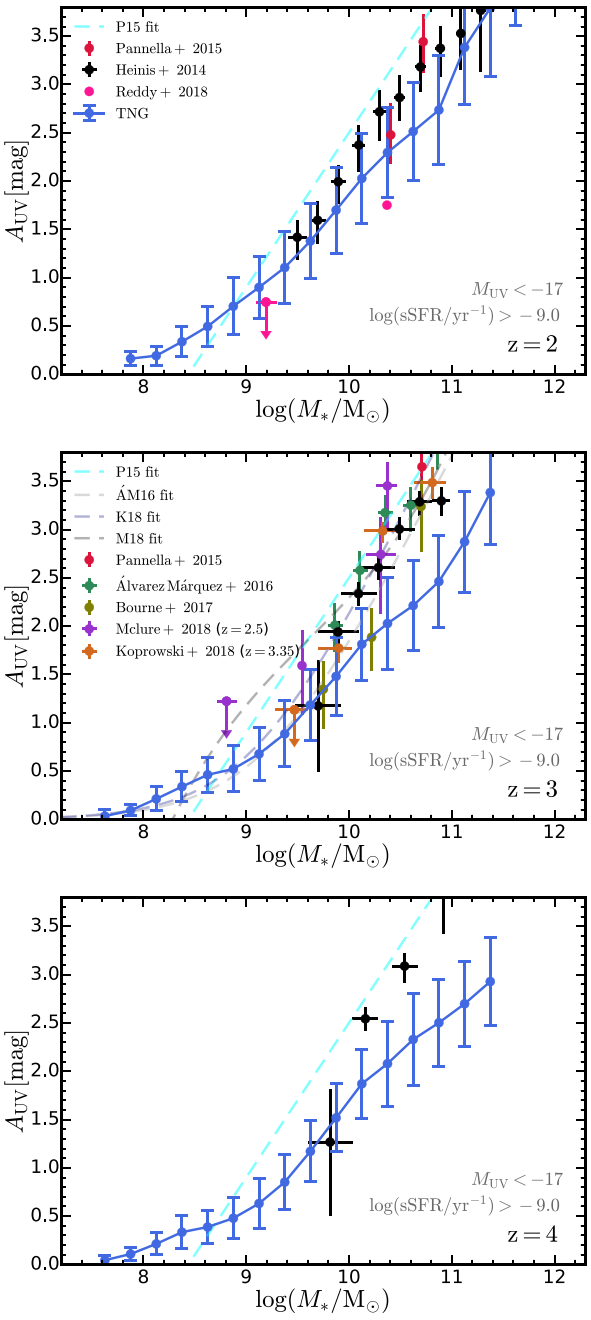

Figure 10. Predicted resolved dust attenuation in the rest-frame UV, A_{UV}, versus stellar mass relations at $z = 2-4$ from the IllustrisTNG simulations. We use the term 'resolved dust attenuation' because the unresolved dust component in the MAPPINGS-III SED library is always present and cannot be subtracted. However, we note that the impact of the unresolved dust attenuation on galaxy continuum emission is limited. Here, we select only star-forming galaxies with $\log(\mathrm{sSFR/yr^{-1}}) > -9.0$ and rest-frame UV magnitude $M_{\mathrm{UV}} < -17$. We compare our results with observations from Heinis et al. (2014), Pannella et al. (2015), Álvarez-Márquez et al. (2016), Bourne et al. (2017), Koprowski et al. (2018), McLure et al. (2018), and Reddy et al. (2018). The fitted relations in observations are shown as the dashed lines. The predictions are consistent with observations at the low-mass end despite the underprediction of A_{UV} at the massive end.

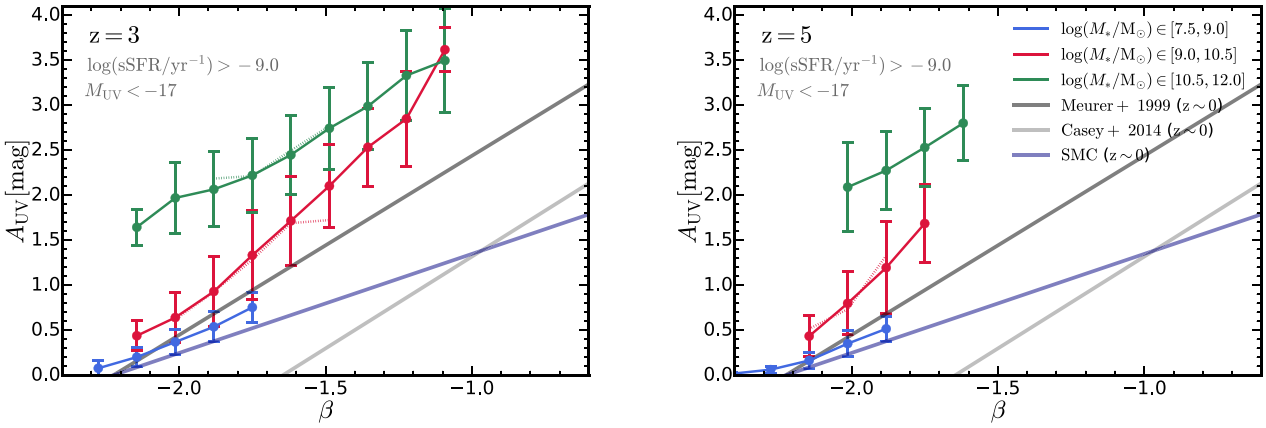

Figure 11. Predicted $A_{\rm UV}$ versus β relations at $z = 3$, 5 from the IllustrisTNG simulations. Here, we select only star-forming galaxies with log (sSFR/yr^{-1}) > -9.0 and rest-frame UV magnitude $M_{\rm UV} < -17$. We divide galaxies into three stellar mass bins: log (M_*/ M$_\odot$) ∈ [7.5, 9.0], [9.0, 10.5], [10.5, 12.0], and evaluate the $A_{\rm UV}-\beta$ relation in each stellar mass bin. The blue circles with the error bars and the blue solid lines show the median relation with 1σ dispersion in the log (M_*/ M$_\odot$) ∈ [7.5, 9.0] bin from TNG50. The red solid lines show the relation in the log (M_*/ M$_\odot$) ∈ [9.0, 10.5] bin from TNG100. We also present the relation in the same stellar mass bin from TNG50 with the red-dotted lines, which almost overlaps with the one from TNG100. This indicates that the stellar mass does control the $A_{\rm UV}-\beta$ relation. Similarly, we show the relation in the log (M_*/ M$_\odot$) ∈ [10.5, 12.0] bin from TNG300 with the green solid lines and the relation in the same stellar mass bin from TNG100 with the green-dotted lines. These results are compared with the canonical relations (Meurer et al. 1999; Casey et al. 2014). We find that the $A_{\rm UV}-\beta$ relations predicted at high redshifts generally lie at higher positions (stronger attenuation or bluer continuum) on the $A_{\rm UV}-\beta$ plane than the canonical relations. The $A_{\rm UV}-\beta$ relations of more massive galaxies tend to lie at higher positions.

1σ dispersion for each stellar mass bin. For the log (M_*/ M$_\odot$) ∈ [7.5, 9.0] bin, we show the relation of TNG50 galaxies as the blue solid lines. For the log (M_*/ M$_\odot$) ∈ [9.0, 10.5] bin, we show the relation of TNG100 galaxies as the red solid lines and the relation of TNG50 galaxies as the red-dotted lines. For the log (M_*/ M$_\odot$) ∈ [10.5, 12.0] bin, we show the relation of TNG300 galaxies as the green solid lines and the relation of TNG100 galaxies as the green-dotted lines. We compare our results with the canonical relations measured in the local Universe: the Meurer et al. (1999) relation, the Casey et al. (2014) relation, and the SMC relation derived in Bouwens et al. (2016). The median relations for the same stellar mass bin from different simulations overlap, which indicates that the stellar mass does control the $A_{\rm UV}-\beta$ relation. The slope of the $A_{\rm UV}-\beta$ relation is shallower in the high and low stellar mass bins. The relation in the intermediate stellar mass bin lies above the canonical Meurer et al. (1999) relation while its slope is close to the Meurer et al. (1999) relation. The relation in the low stellar mass bin lies below the relation derived in the intemediate mass bin and its slope is close to the SMC relation. Galaxies in the high stellar mass bin that encounter the strongest dust attenuation lie significantly above all the canonical relations in the local Universe. In observations, a consistent picture has emerged in the local Universe. Metal and dust poor galaxies tend to have the SMC-like $A_{\rm UV}-\beta$ relation with redder UV continuum and less dust, which corresponds to the simulated galaxies in the low stellar mass bin; normal star-forming galaxies as those in the intermediate-mass bin exhibit the canonical relations (e.g. Buat et al. 2005, 2010; Seibert et al. 2005; Cortese et al. 2006; Muñoz-Mateos et al. 2009; Takeuchi et al. 2010; Hao et al. 2011; Overzier et al. 2011; Boquien et al. 2012). IR luminous galaxies were found to lie significantly above the canonical relations (e.g. Goldader et al. 2002; Buat et al. 2005; Burgarella, Buat & Iglesias-Páramo 2005; Howell et al. 2010; Takeuchi et al. 2010). A systematic study at $z = 0-3.5$ by Casey et al. (2014) showed that galaxies will lie at higher position on the $A_{\rm UV}-\beta$ plane if they have higher rest-frame IR luminosity (more dusty) or higher rest-frame UV luminosity, which is consistent with what we find in the high stellar mass bin. Due to the complexity in the $A_{\rm UV}-\beta$ relation, one should be cautious in using β as a dust attenuation indicator. The inferred $A_{\rm UV}$ from the same β can differ up to ∼1 dex for galaxies with different stellar masses. This can result in large systematic discrepancies in predicting the dust attenuated galaxy luminosities. For example, in Model A of Paper I, we have adopted an empirical dust attenuation model that utilizes the $A_{\rm UV}-\beta$ relation and the $\beta-M_{\rm UV}$ relation measured in observations. We found that the canonical $A_{\rm UV}-\beta$ relation underpredicted dust attenuation at the bright end, while overpredicted the dust attenuation at the faint end. There we had to manually increase the slope of the $\beta-M_{\rm UV}$ relation to make the predicted galaxy rest-frame UV luminosity functions consistent with observations.

For the redshift dependence of the $A_{\rm UV}-\beta$ relation, most of the predicted relations at high redshift lie significantly above the local canonical relations measured in the Local Universe. Similar phenomena have been found in observations. Galaxies at high redshift tend to lie above or on the bluer side of the canonical relations measured in the local Universe (e.g. Howell et al. 2010; Penner et al. 2012; Reddy et al. 2012; Casey et al. 2014; Schulz et al. 2020). However, we do not find apparent redshift evolution of the $A_{\rm UV}-\beta$ relation at $z = 3$, 5. Both the normalizations and the slopes of the relations in different stellar mass bins are stable at $z = 3$, 5, despite that the population of UV red galaxies (with high βs) gradually diminishes at higher redshift.

The location of galaxies on the $A_{\rm UV}-\beta$ plane is conjectured to be affected by the star formation history and the stellar metallicities of galaxies (e.g. Kong et al. 2004; Muñoz-Mateos et al. 2009; Narayanan et al. 2018; Schulz et al. 2020). Older stellar populations or higher stellar metallicities can drive the relation downwards due to the reddening of galaxy intrinsic SEDs. This would explain why high-redshift galaxies generally lie above the local relations since they are more dominated by young stellar populations. But the

systematic dependence of the $A_{\rm UV}-\beta$ on galaxy stellar mass would not be simply explained by the differences in galaxy intrinsic SEDs. Supported by the fact that the intrinsic β has almost no dependence on galaxy rest-frame UV luminosity as shown in Fig. 9, the mass dependence of the $A_{\rm UV}-\beta$ relation of the simulated galaxies is not mainly driven by the intrinsic properties of the stellar populations. We note that this argument may not be true for selected subsamples of galaxies, the $A_{\rm UV}-\beta$ relation of which can still strongly depend on the intrinsic properties of the stellar populations. Alternatively, some studies attribute the complexity in the $A_{\rm UV}-\beta$ relation to the differences in dust attenuation curves (e.g. Gordon et al. 2000; Burgarella et al. 2005; Boquien et al. 2009; Narayanan et al. 2018; Álvarez-Márquez et al. 2019; Ma et al. 2019) and dust geometry (e.g. Seibert et al. 2005; Cortese et al. 2006; Boquien et al. 2009; Narayanan et al. 2018). For example, optically thin UV sightlines in galaxies with complex geometries would result in a bluer UV continuum. On the other hand, steep SMC-like attenuation curves would result in a redder UV continuum. We defer the discussion of the dust attenuation curve and dust geometry to the next section.

In the top panel of Fig. 12, we provide a detailed comparison between the predicted $A_{\rm UV}-\beta$ relation with observations at $z \simeq 3$ (Álvarez-Márquez et al. 2016; Koprowski et al. 2018; McLure et al. 2018) and the canonical relations (Meurer et al. 1999; Casey et al. 2014). In matching the stellar masses of the selected galaxies in observations ($\sim 10^{10}\,{\rm M}_\odot$), we choose a stellar mass bin $\log(M_*/{\rm M}_\odot) \in [9.5, 10.5]$ and correspondingly choose TNG100 to make the comparison. Here, we have also restricted our analysis to star-forming galaxies with rest-frame UV magnitude $M_{\rm UV} < -17$. We switch the selection criterion on sSFR between $\log({\rm sSFR/yr^{-1}}) > -9.0$ and $\log({\rm sSFR/yr^{-1}}) > -9.5$ and show the results with the two criteria explicitly. The prediction is in reasonable agreement with these observations at 1σ level and lies above the local canonical relation (Meurer et al. 1999). The relations derived with different selection criteria overlap. The selection with the lower sSFR threshold -9.5 tends to include galaxies with high βs, but choosing a sSFR threshold lower than -9.5 would not change the relation further. In the bottom panel, we compare the relations derived with different methods for calculating β and with different wavelength range choices. We use the $\log({\rm sSFR/yr^{-1}}) > -9.5$ selection criterion here to make the visual comparison clearer. Our fiducial method is fitting the SED from 1450 to 3000 Å with a power law. Alternatively, we experiment with determining β purely by the flux measured by two top-hat filters at the head and the end of the wavelength range, referred to as the photometric approach and denoted with 'phot'. We also experiment with two other wavelength range choices: 1450 to 2000 Å and 1450 to 2500 Å. Our fiducial approach and wavelength choice produce the result that lies at the centre among all approaches. The photometric approach with 1450 and 3000 Å as the head and the end produces a slightly more consistent result with observations. This is likely because the simulated UV continuum SED does not have a perfect power-law shape but has a dip around 2175 Å caused by the UV bump feature of the dust attenuation curve. Affected by this dip, the SED fitting approach can give relatively lower β compared with the photometric approach.

We note that, across all our analysis on β, there is a deficiency of UV red (with high β) and heavily attenuated galaxies at high redshift in the simulations compared with observations. The deficiency appears in the $A_{\rm UV}-\beta$ relation shown in Figs 11 and 12 where galaxies with $\beta \sim -0.5$ in observations are missing in the simulations. This deficiency is not affected by the selection criteria we choose and it also appears when no selection on sSFR is made. We note that the stellar masses of galaxies selected for Fig. 12 have already been chosen to match the masses of observed galaxies, so the deficiency is also not affected by biases in stellar masses of galaxies. Such a deficiency also manifests in the $A_{\rm UV}-M_*$ relation shown in Fig. 10 where the simulated galaxies at the massive end encounter lower dust attenuation compared with the observed ones. The deficiency could explain the discrepancy we found at the bright end of the $\beta-M_{\rm UV}$ relation shown in Fig. 9.

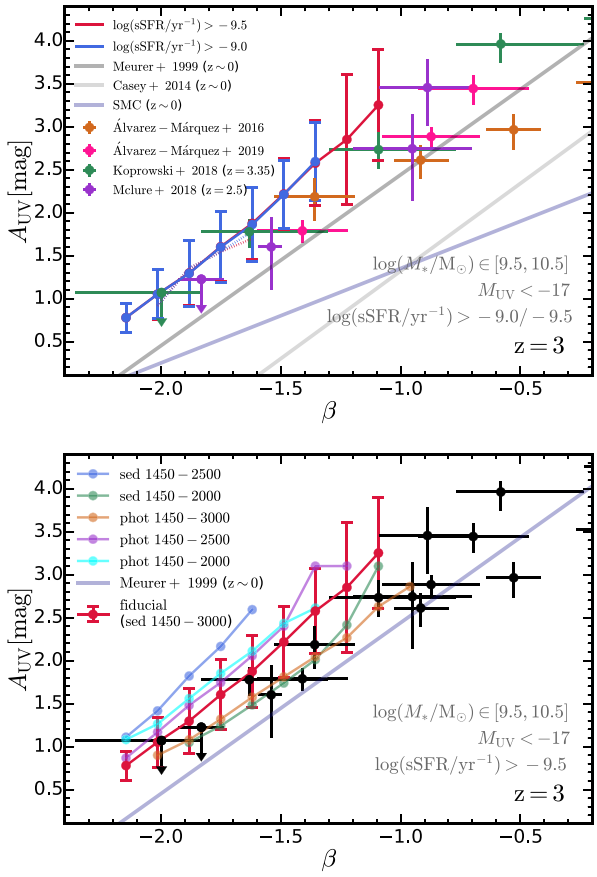

Figure 12. Predicted $A_{\rm UV}$ versus β relations at $z = 3$ from the IllustrisTNG simulations. Top: Predicted $A_{\rm UV}$ versus β relation in stellar mass bin $\log(M_*/{\rm M}_\odot) \in [9.5, 10.5]$. Here, we select only star-forming galaxies with rest-frame UV magnitude $M_{\rm UV} < -17$. We explore the selection criterion on sSFR between $\log({\rm sSFR/yr^{-1}}) > -9.0$ and $\log({\rm sSFR/yr^{-1}}) > -9.5$ and show the results with the two criteria explicitly. We compare the results with selected observations (Álvarez-Márquez et al. 2016; Koprowski et al. 2018; McLure et al. 2018; Álvarez-Márquez et al. 2019) at $z = 3$ that have similar stellar mass binning. We also show canonical relations (Meurer et al. 1999; Casey et al. 2014) with the transparent lines. The predicted relation is in reasonable agreement with observations in this stellar mass restricted comparison. However, there is still a lack of galaxies with $\beta > -1$ in the simulations in this stellar mass bin. The relations derived with different selection criteria overlap. The selection with the higher sSFR threshold -9.5 tends to include galaxies with high βs, but choosing a sSFR threshold lower than -9.5 would not change the relation further. So, the lack of galaxies with $\beta > -1$ is not affected by the selection criterion. Bottom: $A_{\rm UV}$ versus β relations derived with different methods. The label 'sed' indicates SED fitting approach, while 'phot' indicates photometric approach. The prediction from our fiducial approach is shown in the red line. Observational data points are the same as shown in the top panel and are all shown in the black circles here for clarity.

A straight explanation for the deficiency is that we underestimate the dust abundance in massive galaxies. We have simply assumed a constant dust-to-metal ratio among all galaxies at a certain redshift to convert metal abundance to dust abundance. However, some previous studies have revealed that the dust-to-metal ratios increase with the metallicities of galaxies (e.g. Rémy-Ruyer et al. 2014; Popping, Somerville & Galametz 2017; Wiseman et al. 2017; De Vis et al. 2019). Given that more massive galaxies have higher metalicities, we may underestimated the abundance of dust in massive galaxies if we calibrate the model assuming a constant dust-to-metal ratio.

5.5 Dust attenuation curve

The dust attenuation curves describe the wavelength dependence of dust attenuation on galaxy intrinsic emission. As discussed in Model B of Paper I, attenuation is very different from the term extinction (e.g. Calzetti et al. 1994). Extinction only considers the removal of photons from the line of sight. However, attenuation refers to the situation where radiation sources and dust have an extended and complex co-spatial distribution. Photons will not only be removed from the line of sight but can also be scattered into it from other points in the extended source. Therefore, the attenuation curve is seriously affected by the geometrical properties of galaxies and its shape can be very different from the extinction curve.

Modelling the stellar population from the observed galaxy SED requires a robust dust attenuation correction. The resulting physical properties of galaxies, e.g. stellar mass, are greatly influenced by the shape of the assumed dust attenuation curve. The translation between reddening and UV colours also depends on the shape of the dust attenuation curve, which affects the colour selection criteria of galaxies. Moreover, the dust attenuation curves encode physical information on dust grains and are important for studying the cosmic evolution of dust. In many observational and theoretical studies of high-redshift galaxies, a universal attenuation curve has been assumed and the canonical curve measured in local starburst galaxies (Calzetti et al. 2000) has been widely used. However, observations have shown that the dust attenuation curves are far from universal (e.g. Kriek & Conroy 2013; Salmon et al. 2016; Salim, Boquien & Lee 2018; Álvarez-Márquez et al. 2019). For example in Kriek & Conroy (2013), the attenuation curve varies with the spectral shapes of galaxies in Salmon et al. (2016), galaxies at $z = 1.5-3$ with higher colour excess have shallower Calzetti-like attenuation curves and those with lower colour excess have steeper SMC-like attenuation curves, indicating the non-universality of the attenuation curves.

In this paper and Paper I, we have assumed the dust model proposed by Draine & Li (2007), which can reproduce the extinction properties of dust in the Milky Way. So, the potential influence of physical properties of dust on the attenuation curve will not be covered by our analysis. That is to say, if dust is simply placed as a foreground screen to the source, our radiative transfer calculated attenuation curve will be no different from the Milky Way extinction curve. However, the attenuation curve of real galaxies is also influenced by geometrical properties of galaxies. We will focus on this aspect in the subsequent analysis and check to what extent the observed variety of the attenuation curves can be explained purely by dust geometry.

The attenuation curve is usually defined as

$$A_\lambda = k(\lambda)\frac{A_V}{k(\lambda_V)}, \tag{6}$$

where A_V is the attenuation in the V band, which controls the normalization of the curve, and $k(\lambda)$ is a function that controls the shape of the attenuation curve. To compare with the canonical attenuation curve, it is convenient to parametrize $k(\lambda)$ as (e.g. Noll et al. 2009; Kriek & Conroy 2013)

$$k(\lambda) = k^{\rm C}(\lambda)(\lambda/\lambda_V)^\delta, \tag{7}$$

where $k^{\rm C}(\lambda)$ is the Calzetti attenuation curve (Calzetti et al. 2000), δ is a correction factor on the slope of the attenuation curve, and λ_V is the wavelength of the V band. A higher δ indicates a shallower attenuation curve and vice versa. Under this parametrization, we have $k(\lambda_V) = k^{\rm C}(\lambda_V) = 4.05$.

First, we study the dust attenuation curves of star-forming galaxies at different redshifts. We calculate the median attenuation curve for galaxies in TNG50 at $z = 2, 4, 6$ with 'intrinsic' (without the resolved dust attenuation) optical colour $g-r < 0.2$, rest-frame UV magnitude $M_{\rm UV} < -17$ and stellar mass $\log(M_*/{\rm M}_\odot) > 7.5$. We choose these selection criteria because the calculated attenuation curve is valid only when the geometry of the galaxy is properly resolved. We also note that the attenuation calculated here is the resolved dust attenuation. In the top panel of Fig. 13, we show the median attenuation curves of galaxies at $z = 2$, 4, 6 along with a 1σ dispersion. The attenuation curve at $z = 2$ is shallower than the Milky Way extinction curve. This is not surprising considering the complex dust geometry in galaxies. For instance, in the case that stars and dust are uniformly co-spatially mixed, dust attenuation would depend on optical depth as (Calzetti et al. 1994): $A_\lambda = -\frac{2.5}{\ln 10}\ln\left[\frac{1-e^{-\tau(\lambda)}}{\tau(\lambda)}\right]$. Given the same optical depth $\tau(\lambda)$, the attenuation curve here would be shallower than the extinction curve that behaves as $A_\lambda = 2.5/\ln 10\,\tau(\lambda)$. At higher redshift, we find that the attenuation curve becomes steeper and is accompanied by sharp spikes around emission lines. Both of the phenomena can be attributed to dust geometry. As shown in Fig. 7, the origin of the line emission clearly has a spatial correlation with the dust mass distribution in the galaxy. Such a correlation with dust is less apparent in the broad-band galaxy image. Young and massive stars that are responsible for the continuum emission in the UV and the nebular line emission are usually embedded in environments that are rich in cold gas and dust. Therefore, their emission suffers preferentially stronger dust attenuation. Then, in terms of the attenuation curve for the entire galaxy, the attenuation in the UV and the attenuation of emission lines will become relatively higher, resulting in a steeper attenuation curve as well as spikes around emission lines in the curve. Similar phenomena have also been revealed in observations (e.g. Reddy et al. 2015) that the dust attenuation of emission lines was found to be larger than that of the continuum in star-forming galaxies, and the difference can reach as much as a factor $\sim$2 in magnitude. The effect is stronger when the galaxy is richer in dense clumps of cold gas where star formation takes place and is stronger when the stellar population is more dominated by young stars. The steepening of the attenuation curve towards higher redshift can be explained by the younger stellar populations and the stronger star formation in high-redshift galaxies. To make it more clear, we compare the attenuation curves of red and blue galaxies, shown in the bottom panel of Fig. 13. The attenuation curve of red galaxies is clearly shallower than that of blue galaxies.

In observations, the slope correction δ of the attenuation curve was found to have a positive correlation with both stellar mass and colour excess $E(B-V)$, with shallower attenuation curves found in

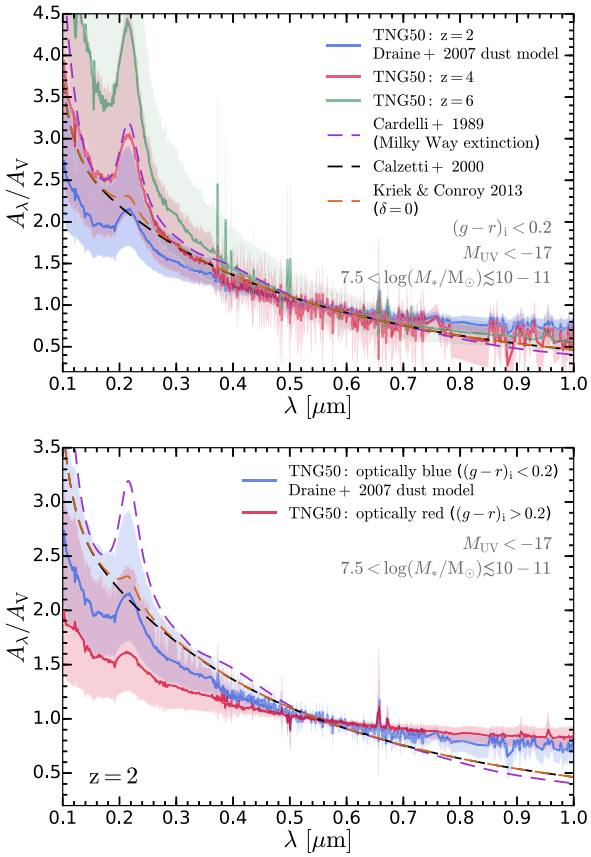

Figure 13. Predictions for the dust attenuation curves from the TNG50 simulation. Top: Dust attenuation curves of galaxies in TNG50 at $z = 2$, 4, 6. Only galaxies with 'intrinsic' (without the resolved dust attenuation) optical colour $g-r < 0.2$, rest-frame UV magnitude $M_{UV} < -17$, and stellar mass $\log(M_*/M_\odot) > 7.5$ are selected. The maximum stellar mass that TNG50 can sample at these redshifts is $\log(M_*/M_\odot) \simeq 10-11$. The solid lines indicate the median dust attenuation at each wavelength, while the shaded regions show 1σ dispersion. The dashed lines show canonical attenuation curves from Cardelli, Clayton & Mathis (1989), Calzetti et al. (2000), and Kriek & Conroy (2013). The dust attenuation curve of galaxies at higher redshift is steeper. Bottom: Dust attenuation curves of blue and red galaxies in TNG50 at $z = 2$. Galaxies with 'intrinsic' optical colour $g-r <$ 0.2 are classified as blue, otherwise red. The dust attenuation curve of blue galaxies is steeper than that of red galaxies.

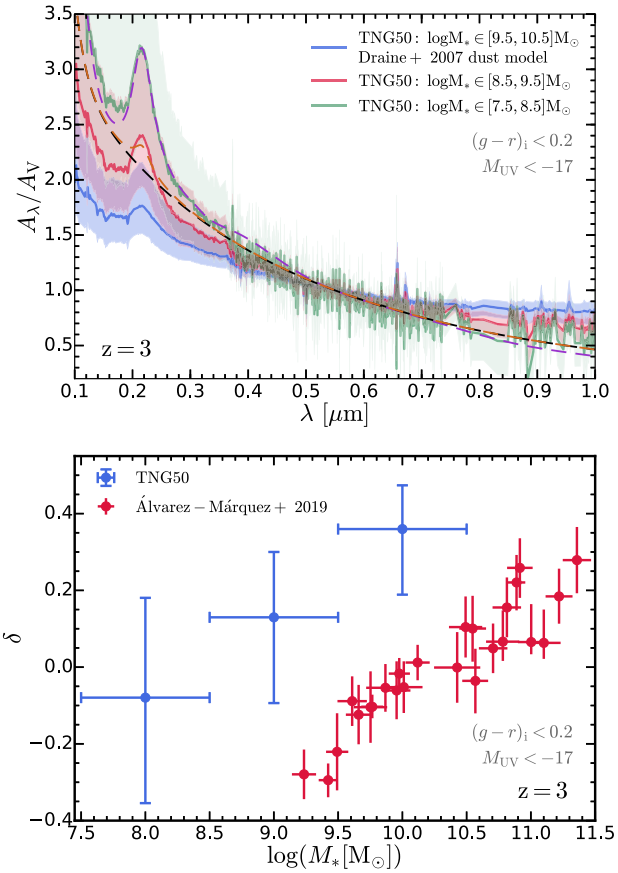

Figure 14. Predictions for the dust attenuation curves from the TNG50 simulation. Top: Dust attenuation curves of galaxies with different stellar masses in TNG50 at $z = 3$. Only galaxies with 'intrinsic' (without the resolved dust attenuation) optical colour $g-r < 0.2$ and rest-frame UV magnitude $M_{UV} < -17$ are selected. We divide galaxies into three stellar mass bins: $\log(M_*/M_\odot) \in$ [7.5, 8.5], [8.5, 9.5], and [9.5,10.5]. The solid lines indicate the median attenuation at each wavelength, while the shaded regions show 1σ dispersion. The dashed lines show canonical attenuation curves from Cardelli et al. (1989), Calzetti et al. (2000), and Kriek & Conroy (2013). The dust attenuation curve of more massive galaxies is shallower. Bottom: Slope correction factor δ (defined in equation 7) versus galaxy stellar mass relation at $z = 3$ compared with the observation from Álvarez-Márquez et al. (2019). We predict a qualitatively consistent trend with the observations. However, the predicted attenuation curves are less steep than the observed ones.

more massive or dusty galaxies (e.g. Salmon et al. 2016; Salim et al. 2018; Álvarez-Márquez et al. 2019). These findings can be explained to some extent by dust geometry. More massive galaxies are usually lower in their sSFR, less dominated by young stellar populations and thus less affected by the differential attenuation of blue emission discussed above. Moreover, the complex dust geometry in massive galaxies gives rise to more optically thin UV sightlines. Emission through these sightlines would suffer much less attenuation in the UV. Both of the two factors drive the attenuation curve shallower in more massive galaxies.

Furthermore, as revealed by the $A_{UV}-M_*$ relation we presented above, more massive galaxies are more heavily attenuated and thus have higher colour excess. So, dust geometry can also qualitatively explain why galaxies with higher colour excess have shallower attenuation curves. We demonstrate these explanations in the top panel of Fig. 14 where the attenuation curves of galaxies in the three different stellar mass bins are presented. The attenuation curves in low-mass galaxies are shallower than those in massive galaxies. We fit the attenuation curves with the formula in equation (7). We neglect the wavelength range from 1500 to 3000 Å; in our fit to avoid the influence of the UV bump feature. The fitted slope correction factor δ as a function of stellar mass is presented in the bottom panel of Fig. 14. Compared with the observational measurements from Álvarez-Márquez et al. (2019), we qualitatively produce a consistent dependence of δ on galaxy stellar mass, while finding a systematic offset $\Delta\delta \simeq 0.4$. In all three stellar mass bins, the attenuation curves are not as steep as the ones found in the observations. This indicates missing factors other than the geometrical properties of galaxies that affect the shape of the attenuation curve. The physical properties of dust grains, e.g. the grain size distribution, the chemical composition, etc. in galaxies at high redshift can be very different from those in the local Universe.

The variety in the dust attenuation curves also plays a role in the complexity of the $A_{\rm UV}-\beta$ relation. A steeper attenuation curve in the UV will result in a redder observed UV continuum with higher β. Galaxies with lower (higher) stellar masses exhibiting steeper (shallower) attenuation curves have higher (lower) UV continuum slope β. This offers an explanation for the dependence of the $A_{\rm UV}-\beta$ relation on galaxy stellar mass explored in Section 5.4. In observations, the shape of the attenuation curves has also been favoured as the main driver of the complexity of the $A_{\rm UV}-\beta$ relation (e.g. Salmon et al. 2016; Lo Faro et al. 2017; Álvarez-Márquez et al. 2019).

6 CONCLUSIONS

In this paper, we have studied properties of galaxy populations at high redshift from the IllustrisTNG simulation suite consisting of TNG50, TNG100, and TNG300. Most importantly, the IllustrisTNG simulations employ a galaxy formation model that produces a realistic low-redshift Universe that is consistent with a wide range of observational data. As introduced in Paper I of this series, galaxies from the simulations were post-processed with full Monte Carlo radiative transfer calculations to model dust attenuation. We have calibrated the dust attenuation model (assuming the Draine & Li (2007) dust mix) based on the galaxy rest-frame UV luminosity functions measured at $z = 2-10$ and have made predictions for the *JWST* apparent bands' luminosity functions in Paper I. In this paper, we focus on providing further predictions for high-redshift galaxies that involve a variety of photometric and spectroscopic features of galaxies. We make comparisons with existing observations and provide predictions that can be tested by future *JWST* observations. Our findings can be summarized as

(i) $M_{\rm halo}-M_{\rm UV}$ relation: The predicted $M_{\rm halo}-M_{\rm UV}$ relation at $z = 4-8$ is consistent with most of the previous theoretical works with $\lesssim$0.3 dex differences in halo masses at all luminosities and redshifts. Dust attenuation plays a crucial role in shaping this relation, producing a steepening at the bright end. We confirm the success of previous empirical models that link galaxy star formation with halo assembly history. However, we find larger scatter in the predicted $M_{\rm halo}-M_{\rm UV}$ relation compared to that predicted by an empirical model (Tacchella et al. 2018). The discrepancy indicates that the halo assembly time is not the only factor that causes the scatter in galaxy–halo scaling relations. The star formation history of a galaxy does not perfectly follow the mass accretion history of its host halo.

(ii) Emission line luminosity functions: We predict the Hα luminosity functions at $z = 2-5$ and derive the best-fitting Schechter function parameters. The evolution of the predicted Hα luminosity function at $z \geq 2$ is consistent with the evolutionary trend found in observations at $z \leq 2.33$. The predicted Hα luminosity function is $\sim$0.3 dex dimmer than the observational binned estimations at $z \simeq 2$. In addition, we make predictions for the Hβ + [O III] luminosity function at $z = 2$, 3, 8 and find good agreement with observational binned estimations at $z \leq 3.2$ with $\lesssim$0.1 dex differences in luminosities. The evolutionary pattern is similar to that of the Hα luminosity function. We calculate the detection limits of a possible future *JWST* observational campaign, assuming a target SNR = 10 and an exposure time $T_{\rm exp} = 10^4$ s. We find that, with the NIRSpec instrument, the Hα line can be detected down to $\sim 10^{41.7}$ erg s^{-1} at $z = 6$ and the Hβ + [O III] line can be detected down to $\sim 10^{42.0}$ erg s^{-1} at $z = 8$. With the *JWST* NIRSpec instrument, ~ 2/arcmin^2 Hβ + [O III] emitters at $z = 8$ are expected to be observed assuming a survey depth $\Delta z = 1$.

(iii) D4000 versus sSFR relation: The predicted D4000 versus sSFR relation at $z = 2$ lies on the local calibrations at the high sSFR end. The galaxies at $z = 2$ distribute systematically in the high sSFR, low D4000 regime compared with local galaxies. This is consistent with the trend found at $z \lesssim 1$ in observations. The distribution pattern of galaxies at $z = 2$ on the D4000–sSFR plane is very different from that of local galaxies. A cluster of star-forming galaxies followed by a tail of passive galaxies shows up instead of the bimodal distribution found in the local Universe. The tail of passive galaxies has lower D4000 at fixed sSFR compared with the local calibration.

(iv) UV continuum slope β: Both the predicted $\beta-M_{\rm UV}$ relation and the $A_{\rm UV}$ versus stellar mass relation are only consistent with observations at the faint (low mass) end. β ($A_{\rm UV}$) is underpredicted at the bright (massive) end. The differences are more apparent at higher redshift and could reach $\sim$1 mag at $\log(M_*/{\rm M}_\odot) \simeq 11$ at $z = 4$. These discrepancies indicate a deficiency of galaxies with high β or strong attenuation in the simulations. We study the $A_{\rm UV}-\beta$ relation in different stellar mass bins at $z = 3$, 5 and find that galaxies with higher (lower) stellar mass lie higher (lower) on the $A_{\rm UV}-\beta$ plane. Such a dependence can systematically explain observational findings for this relation. At the stellar mass similar to that of observed galaxy samples, the predicted $A_{\rm UV}-\beta$ relation is consistent with observations at $z \simeq 3$ at 1σ level.

(v) Dust attenuation curves: We focus on the influence of dust geometry on the shape of the dust attenuation curves of galaxies. We study the dependence of the attenuation curve on redshift, galaxy optical colour, and stellar mass. We find that the attenuation curves are steeper in galaxies at higher redshifts, with lower stellar masses, or bluer optical colours. The dependence can be related to a positive correlation between curve steepness and domination of young stellar populations. The continuum emission at short wavelengths from young stellar populations suffers preferentially stronger dust attenuation in the birth environment of stars, which results in a steeper attenuation curve. Our findings are qualitatively consistent with the observed trend despite that the predicted curves are not as steep as the observed ones. This indicates that the geometrical property of galaxies is not the only factor that affects the shape of the attenuation curve at high redshift.

In this paper, based on the IllustrisTNG simulation suites, using our radiative post-processing technique, we make detailed predictions for galaxy populations at high redshift. These predictions are in the regime that will be studied by future *JWST* observations. In general, our predictions produce 'qualitative' trends that are consistent with observations in all the aspects explored in this paper. Quantitatively, our results are consistent with previous theoretical models on galaxy halo scaling relations and are consistent with existing observations on emission line luminosity functions within $\sim$0.3 dex (a factor of $\sim$2) differences in masses/luminosities. However, at the bright/massive end, our results significantly underpredict the amount of dust attenuation and results in a deficiency of heavily attenuated, UV red galaxies. We also find that dust attenuation curves measured in observations are steeper than predicted. We note that the tensions with observations we found in this paper could be caused by our simplified treatment of dust in the post-processing procedure, e.g. our assumption of the dust model (Draine & Li 2007), and do not necessarily imply that the IllustrisTNG galaxy formation model is flawed. In order to break the degeneracy, a self-consistent treatment of dust as well as the nebular emission and the unresolved dust attenuation will be needed. These aspects will be explored in follow-up works.

ACKNOWLEDGEMENTS

FM acknowledges support through the Program 'Rita Levi Montalcini' of the Italian Ministry of Education, University and Research (MIUR). The primary TNG simulations were realized with compute time granted by the Gauss Centre for Supercomputing (GCS): TNG50 under GCS Large-Scale Project GCS-DWAR (2016; PIs Nelson/Pillepich), and TNG100 and TNG300 under GCS-ILLU (2014; PI Springel) on the GCS share of the supercomputer Hazel Hen at the High Performance Computing Centre Stuttgart. MV acknowledges support through an Massachusetts Institute of Technology (MIT) RSC award, a Kavli Research Investment Fund, National Aeronautics and Space Administration (NASA) Astrophysics Theory Program (ATP) grant NNX17AG29G, and National Science Foundation (NSF) grants AST-1814053, AST-1814259, and AST-1909831.

REFERENCES

Adelberger K. L., Steidel C. C., 2000, ApJ, 544, 218
Álvarez-Márquez J. et al., 2016, A&A, 587, A122
Álvarez-Márquez J., Burgarella D., Buat V., Ilbert O., Pŕez-González P. G., 2019, A&A, 630, A153
Baes M., Verstappen J., De Looze I., Fritz J., Saftly W., Vidal Pérez E., Stalevski M., Valcke S., 2011, ApJS, 196, 22
Barrows R. S., Comerford J. M., Zakamska N. L., Cooper M. C., 2017, ApJ, 850, 27
Behroozi P. S., Conroy C., Wechsler R. H., 2010, ApJ, 717, 379
Behroozi P. S., Wechsler R. H., Conroy C., 2013, ApJ, 770, 57
Blain A. W., Smail I., Ivison R. J., Kneib J.-P., Frayer D. T., 2002, Phys. Rep., 369, 111
Blumenthal G. R., Faber S. M., Primack J. R., Rees M. J., 1984, Nature, 311, 517
Boquien M. et al., 2009, ApJ, 706, 553
Boquien M. et al., 2012, A&A, 539, A145
Bourne N. et al., 2017, MNRAS, 467, 1360
Bouwens R. J. et al., 2003, ApJ, 595, 589
Bouwens R. J. et al., 2009, ApJ, 705, 936
Bouwens R. J. et al., 2010, ApJ, 709, L133
Bouwens R. J. et al., 2012, ApJ, 754, 83
Bouwens R. J. et al., 2014, ApJ, 793, 115
Bouwens R. J. et al., 2016, ApJ, 833, 72
Bouwens R. J., Stefanon M., Oesch P. A., Illingworth G. D., Nanayakkara T., Roberts-Borsani G., Labbé I., Smit R., 2019, ApJ, 880, 25
Brinchmann J., Charlot S., White S. D. M., Tremonti C., Kauffmann G., Heckman T., Brinkmann J., 2004, MNRAS, 351, 1151
Bruzual A. G., 1983, ApJ, 273, 105
Buat V. et al., 2005, ApJ, 619, L51
Buat V. et al., 2010, MNRAS, 409, L1
Buat V. et al., 2012, A&A, 545, A141
Burgarella D., Buat V., Iglesias-Páramo J., 2005, MNRAS, 360, 1413
Calzetti D., Kinney A. L., Storchi-Bergmann T., 1994, ApJ, 429, 582
Calzetti D., Armus L., Bohlin R. C., Kinney A. L., Koornneef J., Storchi-Bergmann T., 2000, ApJ, 533, 682
Camps P., Baes M., 2015, Astron. Comput., 9, 20
Camps P., Baes M., Saftly W., 2013, A&A, 560, A35
Cardelli J. A., Clayton G. C., Mathis J. S., 1989, ApJ, 345, 245
Casey C. M. et al., 2014, ApJ, 796, 95
Ceverino D., Glover S. C. O., Klessen R. S., 2017, MNRAS, 470, 2791
Chevallard J. et al., 2019, MNRAS, 483, 2621
Conroy C., Gunn J. E., 2010, ApJ, 712, 833
Conroy C., Wechsler R. H., Kravtsov A. V., 2007, ApJ, 668, 826
Conroy C., Gunn J. E., White M., 2009, ApJ, 699, 486
Cortese L. et al., 2006, ApJ, 637, 242
Cowley W. I., Baugh C. M., Cole S., Frenk C. S., Lacey C. G., 2018, MNRAS, 474, 2352
da Cunha E. et al., 2015, ApJ, 806, 110
Dayal P., Ferrara A., 2018, Phys. Rep., 780, 1
Dayal P., Dunlop J. S., Maio U., Ciardi B., 2013, MNRAS, 434, 1486
De Barros S., Oesch P. A., Labbé I., Stefanon M., González V., Smit R., Bouwens R. J., Illingworth G. D., 2019, MNRAS, 489, 2355
De Vis P. et al., 2019, A&A, 623, A5
Dolag K., Borgani S., Murante G., Springel V., 2009, MNRAS, 399, 497
Donnari M. et al., 2019, MNRAS, 485, 4817
Draine B. T., Li A., 2007, ApJ, 657, 810
Duncan K. et al., 2014, MNRAS, 444, 2960
Dunlop J. S. et al., 2013, MNRAS, 432, 3520
Endsley R., Behroozi P., Stark D. P., Williams C. C., Robertson B. E., Rieke M., Gottlöber S., Yepes G., 2020, MNRAS, 493, 1178
Eyles L. P., Bunker A. J., Stanway E. R., Lacy M., Ellis R. S., Doherty M., 2005, MNRAS, 364, 443
Fang J. J. et al., 2018, ApJ, 858, 100
Finkelstein S. L., 2016, Publ. Astron. Soc. Aust., 33, e037
Finkelstein S. L. et al., 2012, ApJ, 756, 164
Finkelstein S. L. et al., 2015, ApJ, 810, 71
Gardner J. P. et al., 2006, Space Sci. Rev., 123, 485
Garn T. et al., 2010, MNRAS, 402, 2017
Genel S. et al., 2014, MNRAS, 445, 175
Goldader J. D., Meurer G., Heckman T. M., Seibert M., Sanders D. B., Calzetti D., Steidel C. C., 2002, ApJ, 568, 651
González V., Labbé I., Bouwens R. J., Illingworth G., Franx M., Kriek M., Brammer G. B., 2010, ApJ, 713, 115
Gordon K. D. et al., 2000, ApJ, 544, 859
Greene T. P. et al., 2017, J. Astron. Telesc. Instrum. Syst., 3, 035001
Groves B., Dopita M. A., Sutherland R. S., Kewley L. J., Fischera J., Leitherer C., Brandl B., van Breugel W., 2008, ApJS, 176, 438
Haines C. P. et al., 2017, A&A, 605, A4
Hao C.-N., Kennicutt R. C., Johnson B. D., Calzetti D., Dale D. A., Moustakas J., 2011, ApJ, 741, 124
Hathi N. P., Malhotra S., Rhoads J. E., 2008, ApJ, 673, 686
Hayes M., Schaerer D., Östlin G., 2010, A&A, 509, L5
Heinis S. et al., 2014, MNRAS, 437, 1268
Hodge J. A. et al., 2013, ApJ, 768, 91
Hopkins P. F. et al., 2018, MNRAS, 480, 800
Howell J. H. et al., 2010, ApJ, 715, 572
Ibar E. et al., 2013, MNRAS, 434, 3218
Inami H. et al., 2017, A&A, 608, A2
Ishigaki M., Kawamata R., Ouchi M., Oguri M., Shimasaku K., Ono Y., 2018, ApJ, 854, 73
Johnston R., Vaccari M., Jarvis M., Smith M., Giovannoli E., Häußler B., Prescott M., 2015, MNRAS, 453, 2540
Jonsson P., Groves B. A., Cox T. J., 2010, MNRAS, 403, 17
Kauffmann G. et al., 2003, MNRAS, 341, 33
Kennicutt R. C., Jr., 1998, ARA&A, 36, 189
Khostovan A. A., Sobral D., Mobasher B., Best P. N., Smail I., Stott J. P., Hemmati S., Nayyeri H., 2015, MNRAS, 452, 3948
Kimm T., Cen R., 2013, ApJ, 776, 35
Kong X., Charlot S., Brinchmann J., Fall S. M., 2004, MNRAS, 349, 769
Koprowski M. P. et al., 2018, MNRAS, 479, 4355
Kriek M., Conroy C., 2013, ApJ, 775, L16
Kriek M., van Dokkum P. G., Whitaker K. E., Labbé I., Franx M., Brammer G. B., 2011, ApJ, 743, 168
Kriek M. et al., 2015, ApJS, 218, 15
Lee J. C. et al., 2012, PASP, 124, 782
Leja J. et al., 2019, ApJ, 877, 140
Lo Faro B., Buat V., Roehlly Y., Alvarez-Marquez J., Burgarella D., Silva L., Efstathiou A., 2017, MNRAS, 472, 1372
Ma X. et al., 2018, MNRAS, 478, 1694
Ma X. et al., 2019, MNRAS, 487, 1844
Madau P., 1995, ApJ, 441, 18
Madau P., Dickinson M., 2014, ARA&A, 52, 415
Madau P., Ferguson H. C., Dickinson M. E., Giavalisco M., Steidel C. C., Fruchter A., 1996, MNRAS, 283, 1388

Marchesini D., van Dokkum P. G., Förster Schreiber N. M., Franx M., Labbé I., Wuyts S., 2009, ApJ, 701, 1765
Marinacci F. et al., 2018, MNRAS, 480, 5113
Mason C. A., Trenti M., Treu T., 2015, ApJ, 813, 21
Matthee J., Sobral D., Best P., Smail I., Bian F., Darvish B., Röttgering H., Fan X., 2017, MNRAS, 471, 629
McLure R. J., Cirasuolo M., Dunlop J. S., Foucaud S., Almaini O., 2009, MNRAS, 395, 2196
McLure R. J. et al., 2013, MNRAS, 432, 2696
McLure R. J. et al., 2018, MNRAS, 476, 3991
Meurer G. R., Heckman T. M., Lehnert M. D., Leitherer C., Lowenthal J., 1997, AJ, 114, 54
Meurer G. R., Heckman T. M., Calzetti D., 1999, ApJ, 521, 64
Mobasher B. et al., 2015, ApJ, 808, 101
Moster B. P., Naab T., White S. D. M., 2013, MNRAS, 428, 3121
Muñoz-Mateos J. C. et al., 2009, ApJ, 701, 1965
Murphy E. J. et al., 2011, ApJ, 737, 67
Naiman J. P. et al., 2018, MNRAS, 477, 1206
Narayanan D., Davé R., Johnson B. D., Thompson R., Conroy C., Geach J., 2018, MNRAS, 474, 1718
Nelson D. et al., 2015, Astron. Comput., 13, 12
Nelson D. et al., 2018, MNRAS, 475, 624
Nelson D. et al., 2019a, MNRAS, 490, 3234
Nelson D. et al., 2019b, Comput. Astrophys. Cosmol., 6, 2
Noll S., Burgarella D., Giovannoli E., Buat V., Marcillac D., Muñoz-Mateos J. C., 2009, A&A, 507, 1793
Oesch P. A. et al., 2010, ApJ, 709, L16
Oesch P. A., Bouwens R. J., Illingworth G. D., Labbé I., Stefanon M., 2018, ApJ, 855, 105
Ouchi M. et al., 2004, ApJ, 611, 660
Ouchi M. et al., 2009, ApJ, 706, 1136
Overzier R. A. et al., 2011, ApJ, 726, L7
Paardekooper J.-P., Khochfar S., Dalla C. V., 2013, MNRAS, 429, L94
Pakmor R., Springel V., Bauer A., Mocz P., Munoz D. J., Ohlmann S. T., Schaal K., Zhu C., 2016, MNRAS, 455, 1134
Pannella M. et al., 2009, ApJ, 698, L116
Pannella M. et al., 2015, ApJ, 807, 141
Papovich C., Dickinson M., Ferguson H. C., 2001, ApJ, 559, 620
Papovich C. et al., 2004, ApJ, 600, L111
Penner K. et al., 2012, ApJ, 759, 28
Pillepich A. et al., 2018a, MNRAS, 473, 4077
Pillepich A. et al., 2018b, MNRAS, 475, 648
Pillepich A. et al., 2019, MNRAS, 490, 3196
Planck Collaboration XIII, 2016, A&A, 594, A13
Pontoppidan K. M. et al., 2016, in Peck A. B., Seaman R. L., Benn C. R., eds, Proc. SPIE Conf. Ser. Vol. 9910, Observatory Operations: Strategies, Processes, and Systems VI. SPIE, Bellingham, p. 991016
Popping G., Somerville R. S., Galametz M., 2017, MNRAS, 471, 3152
Reddy N. et al., 2012, ApJ, 744, 154
Reddy N. A., Erb D. K., Pettini M., Steidel C. C., Shapley A. E., 2010, ApJ, 712, 1070
Reddy N. A. et al., 2015, ApJ, 806, 259
Reddy N. A. et al., 2018, ApJ, 853, 56
Rémy-Ruyer A. et al., 2014, A&A, 563, A31
Rodriguez-Gomez V. et al., 2018, MNRAS, 483, 4140
Rosdahl J. et al., 2018, MNRAS, 479, 994
Saftly W., Baes M., Camps P., 2014, A&A, 561, A77
Salim S., Boquien M., Lee J. C., 2018, ApJ, 859, 11
Salmon B. et al., 2015, ApJ, 799, 183
Salmon B. et al., 2016, ApJ, 827, 20
Santini P. et al., 2015, ApJ, 801, 97
Santini P. et al., 2017, ApJ, 847, 76
Schaerer D., de Barros S., 2009, A&A, 502, 423
Schulz S., Popping G., Pillepich A., Nelson D., Vogelsberger M., Marinacci F., Hernquist L., 2020, preprint (arXiv:2001.04992)
Seibert M., Heckman T. M., Meurer G. R., 2002, AJ, 124, 46
Seibert M. et al., 2005, ApJ, 619, L55
Shapley A. E., 2011, ARA&A, 49, 525
Shimizu I., Inoue A. K., Okamoto T., Yoshida N., 2014, MNRAS, 440, 731
Sijacki D., Vogelsberger M., Genel S., Springel V., Torrey P., Snyder G. F., Nelson D., Hernquist L., 2015, MNRAS, 452, 575
Simpson J. M. et al., 2014, ApJ, 788, 125
Simpson J. M. et al., 2015, ApJ, 799, 81
Sobral D., Best P. N., Matsuda Y., Smail I., Geach J. E., Cirasuolo M., 2012, MNRAS, 420, 1926
Sobral D., Smail I., Best P. N., Geach J. E., Matsuda Y., Stott J. P., Cirasuolo M., Kurk J., 2013, MNRAS, 428, 1128
Sobral D. et al., 2015, MNRAS, 451, 2303
Solomon P. M., Vanden Bout P. A., 2005, ARA&A, 43, 677
Song M. et al., 2016, ApJ, 825, 5
Speagle J. S., Steinhardt C. L., Capak P. L., Silverman J. D., 2014, ApJS, 214, 15
Springel V., 2010, MNRAS, 401, 791
Springel V., White S. D. M., Tormen G., Kauffmann G., 2001, MNRAS, 328, 726
Springel V. et al., 2018, MNRAS, 475, 676
Stanway E. R., Bunker A. J., McMahon R. G., 2003, MNRAS, 342, 439
Stark D. P., 2016, ARA&A, 54, 761
Stark D. P., Schenker M. A., Ellis R., Robertson B., McLure R., Dunlop J., 2013, ApJ, 763, 129
Steidel C. C. et al., 2014, ApJ, 795, 165
Stott J. P. et al., 2013, MNRAS, 436, 1130
Strom A. L., Steidel C. C., Rudie G. C., Trainor R. F., Pettini M., Reddy N. A., 2017, ApJ, 836, 164
STScI, 2018, Space Telescope Science Institute - JWST User Documentation
Tacchella S., Trenti M., Carollo C. M., 2013, ApJ, 768, L37
Tacchella S., Bose S., Conroy C., Eisenstein D. J., Johnson B. D., 2018, ApJ, 868, 92
Takeuchi T. T., Buat V., Heinis S., Giovannoli E., Yuan F.-T., Iglesias-Páramo J., Murata K. L., Burgarella D., 2010, A&A, 514, A4
Tomczak A. R. et al., 2016, ApJ, 817, 118
Torrey P., Vogelsberger M., Genel S., Sijacki D., Springel V., Hernquist L., 2014, MNRAS, 438, 1985
Trac H., Cen R., Mansfield P., 2015, ApJ, 813, 54
Vogelsberger M., Genel S., Sijacki D., Torrey P., Springel V., Hernquist L., 2013, MNRAS, 436, 3031
Vogelsberger M. et al., 2014a, MNRAS, 444, 1518
Vogelsberger M. et al., 2014b, Nature, 509, 177
Vogelsberger M. et al., 2019, MNRAS, 492, 5167
Wechsler R. H., Tinker J. L., 2018, ARA&A, 56, 435
Weinberger R. et al., 2017, MNRAS, 465, 3291
Weiß A. et al., 2009, ApJ, 707, 1201
White S. D. M., Rees M. J., 1978, MNRAS, 183, 341
Wilkins S. M., Bunker A. J., Ellis R. S., Stark D., Stanway E. R., Chiu K., Lorenzoni S., Jarvis M. J., 2010, MNRAS, 403, 938
Wilkins S. M. et al., 2013, MNRAS, 435, 2885
Wilkins S. M., Feng Y., Di-Matteo T., Croft R., Stanway E. R., Bunker A., Waters D., Lovell C., 2016, MNRAS, 460, 3170
Wilkins S. M., Feng Y., Di Matteo T., Croft R., Lovell C. C., Waters D., 2017, MNRAS, 469, 2517
Williams C. C. et al., 2018, ApJS, 236, 33
Wiseman P., Schady P., Bolmer J., Krühler T., Yates R. M., Greiner J., Fynbo J. P. U., 2017, A&A, 599, A24
Wu X., Davé R., Tacchella S., Lotz J., 2020, MNRAS, 494, 5636
Wuyts S. et al., 2011, ApJ, 738, 106
Xu H., Wise J. H., Norman M. L., Ahn K., O'Shea B. W., 2016, ApJ, 833, 84
Yan H., Windhorst R. A., Cohen S. H., 2003, ApJ, 585, L93
Yung L. Y. A., Somerville R. S., Popping G., Finkelstein S. L., Ferguson H. C., Davé R., 2019a, MNRAS, 490, 2855
Yung L. Y. A., Somerville R. S., Finkelstein S. L., Popping G., Davé R., 2019b, MNRAS, 483, 2983

This paper has been typeset from a TEX/LATEX file prepared by the author.